Made-to-measure Modelling of Nuclear Star Clusters

Samuel W. F. Earp

A thesis submitted in partial fulfilment for the requirements for the degree of *Master of Science* at the University of Central Lancashire.

September 2014

Declaration

I declare that while registered as a candidate for the research degree, I have not been a registered candidate or enrolled student for another award of the University or other academic or professional institution. I declare that no material contained in the thesis has been used in any other submission for an academic award and is solely my own work.

Samuel W. F. Earp

August 2014

To my loving mother and sister, to you I owe everything.

Contents

Contents

List of Figures

List of Tables

Acknowledgements

Abstract

The nuclear star clusters of late-type spiral galaxies are comprised of multiple components. Gemini near-infrared spectroscopy of the nuclear star cluster in NGC 4244 shows clear rotation. Earlier, De Lorenzi et al. (2013) constructed two component (disc + spheroid) axisymmetric three integral particle models of NGC 4244, finding a negative vertical anisotropy ($\beta_z < 0$). We construct a series of axisymmetric, single-component, particle models of NGC 4244 using these data, combined with F814W band photometric data from the Hubble space telescope and the χ^2-made-to-measure code NMAGIC. We find a best fitting central black hole mass of $5 \times 10^5 \, M_\odot$. Our models also have a negative β_z, as in earlier models. We conclude that although the disc component of NGC 4244's nuclear star cluster is clearly present, it has a negligible effect on the measured kinematics. We also present a preliminary density model for the nuclear star cluster residing in the pure spiral galaxy M33.

Chapter 1

Introduction

1.1 Central Objects

The galactic centre is usually the densest region of an entire galaxy. Sitting at the bottom of a galaxy's potential well, the conditions of the central region are extreme. These conditions give rise to a plethora of different objects that reside at the galactic centre. The largest galaxies in the universe often contain black holes at their centre that are extremely massive and are therefore called supermassive black holes (SMBHs). Smaller galaxies often host a nuclear star cluster (NSC) and, on larger scales, a nuclear disc. These objects can also coexist in some galaxies. The Milky Way is a prime example, which may contain all three of these objects.

Deriving the Mass Enclosed by a Circular Orbit

For a particle at radius r, with tangential velocity $\boldsymbol{\upsilon}$ and mass m, the force required to maintain a circular orbit (centripetal force) is given by

$$F = \frac{m\boldsymbol{\upsilon}^2}{r}.$$ (1.1.1)

The force acting on the particle is the force due to gravity. Therefore, we can write

$$F = \frac{GMm}{r^2} = \frac{m\boldsymbol{v}^2}{r}, \tag{1.1.2}$$

where M is the mass of the central object, and G is the gravitational constant. Rearranging equation (1.1.2) yields an expression for the mass enclosed by the circular orbit, M,

$$\boldsymbol{v}^2 = \frac{GM}{r}, \tag{1.1.3a}$$

$$\Rightarrow \ M = \frac{\boldsymbol{v}^2 r}{G}. \tag{1.1.3b}$$

Thus, from just the velocity of the particle and the radius of its orbit, we can determine the mass enclosed. Although sometimes the tangential velocity is not known, therefore, we replace $\boldsymbol{v}$ with the angular velocity $\boldsymbol{\omega}$. By the substitution of $\boldsymbol{v} = \boldsymbol{\omega} r$ we obtain the equation,

$$M = \frac{\boldsymbol{\omega}^2 r^3}{G}. \tag{1.1.4}$$

1.1.1   Supermassive Black Holes

Most of the galaxies we observe in the universe host a central black hole that lies at the bottom of the potential well. These SMBHs have masses greater than $10^6 \, \mathrm{M}_\odot$ and are found in a variety of Hubble types. The largest SMBH to be discovered so far was in the compact lenticular galaxy NGC 1277 (van den Bosch et al. 2012)[97]; this SMBH has a mass of $(1.7 \pm 0.3) \times 10^{10} \, \mathrm{M}_\odot$. The most readily available example of a galaxy that harbours a SMBH at its centre is our own Galaxy, the Milky Way. Lyden-Bell & Rees (1974)[63] first hypothesised the existence of SMBHs as a way of explaining the galactic nucleus of the large class of galaxies known as quasars. These quasars were thought to be stars that were emitting a large amount of radiation. However, when their spectra was analysed it was found

they were, in fact, large galaxies at high redshifts. Just 3 years later Balick & Brown (1974)[2] discovered Sagittarius A-star (Sgr A*). Sgr A* is a compact source of radio emission at the centre of the Milky Way and is believed to be the location of the Milky Way's SMBH. Since Sgr A*s discovery, SMBHs have been found in many galaxies, usually with the help of data obtained from the Hubble Space Telescope (*HST*). It was originally thought that SMBHs were only found in early-types and late-types with bulges, however, Barth et al. (2009)[3] found an exception to this. NGC 3621 is a bulgeless late-type galaxy that was found to contain both a SMBH of mass $\leq 10^7 \, M_\odot$ and a nuclear star cluster (Barth et al. 2009)[3]. One problem facing the discovery of more SMBHs in the centre of bulgeless galaxies is that without dynamically modelling the centre of these galaxies, the SMBH can only be detected when accreting matter. However, not all galaxies host a SMBH, an example of this is the late-type galaxy M33 (Merrit et al. 2001; Gebhardt et al. 2001)[38,71].

Fig. 1.1 Very Large Telescope (VLT) I, V and B band composite image of NGC 3621. *Image credit: ESO*

Numerous relationships between SMBHs and their host galaxies have been proposed. One of the first relationships to be proposed were on the basis of 8 measurements; Kormendy & Richstone (1995)[58] found that the mass of the SMBH scaled linearly with the absolute blue luminosity of the host bulge. This was confirmed by Magorrian et al. (1998)[67] who found a similar relationship using a sample of 30 galaxies. Further work done by Ferrarese & Merritt (2000) and Gebhardt et al. (2000)[36,37] investigated a relationship between SMHB mass and luminosity-weighted line-of-sight velocity dispersion within the half-light radius. Ferrarese & Merritt (2000)[36] used a sample of 12 galaxies to investigate this relationship, their results indicated a strong correlation between the mass of the SMBH and the velocity dispersion of the host galaxy (the M_{SMBH}–σ relation). This correlation can be given explicitly as

$$\log_{10}(M_{SMBH}) = \alpha_\sigma + \beta_\sigma \log_{10}[\sigma/(200)], \qquad (1.1.5)$$

where σ is the velocity dispersion and with the values $\alpha_\sigma = -0.6 \pm 1.3$ and $\beta_\sigma = 4.8 \pm 0.54$. Gebhardt et al. (2000)[37] fitted a sample of 26 galaxies with well determined line-of-sight velocity dispersions, with SMBH masses determined by stellar kinematics and with three-integral models of Hubble Space Telescope (*HST*) spectroscopy. Their sample also included two galaxies whose SMBH masses were obtained via maser dynamical estimates (NGC 4258 and NGC 1068). They found that the correlation between velocity dispersion and SMBH mass is extremely strong, with a correlation coefficient of 0.93. The scatter of SMBH mass at fixed velocity dispersion is 0.3 dex, however the intrinsic scatter given the likely measurement errors was found to be less than 0.15 dex, the correlation is given by

$$\log_{10}(M_{SMBH}) = \alpha_\sigma + \beta_\sigma \log_{10}[\sigma/(200)], \qquad (1.1.6)$$

with the values $\alpha_\sigma = 8.1 \pm 1.54$ and $\beta_\sigma = 3.75 \pm 0.3$. Marconi & Hunt 2003[68] investigated the relationship between the mass of the SMBH and the mass of the bulge. The authors

find a strong correlation with an intrinsic scatter of 0.15 dex. A study by Gultekin et al. (2009)[47] suggests that the relationship between SMBH mass and velocity dispersion may be tighter, i.e. has less intrinsic scatter, than the relationship between black hole mass and bulge mass (or total stellar mass). However, Kormendy et al. (2011)[56] showed that the masses of SMBHs in disc galaxies, do not correlate with their host galaxy.

One problem facing the study of SMBHs is that it can be extremely hard to accurately measure their mass. Only a few galaxies (~ 80) have had their central black hole mass measured (Graham & Scott 2013)[45]. In the Milky Way we have the luxury of being able to resolve the proper motions of stars near the SMBH. These measurements enable us to directly measure the mass of the SMBH (Ghez et al. 2008; Gillessen et al. 2009)[42,43]. Recent work has shown that applying the modelling techniques frequently used to constrain the mass of a central black hole is unreliable. Feldmeier et al. (2014)[34] constructed two integral Jeans models for the Milky Way's NSC. Compared to the dynamical measurements made by Ghez et al. (2008) and Gillessen et al. (2009)[42,43], Feldmeier et al. (2014)[34] found that the best fitting mass for the SMBH was lower by a factor of two.

Intermediate Mass Black Holes

Intermediate mass black holes (IMBHs) are black holes that have a mass in the range of $100 < M_{IMBH} < 10^5 \, \mathrm{M_\odot}$, too massive to be single stars and too small to be SMBHs. IMBHs are generally found in the centre of globular clusters (GCs), for example M3, M13 and M92 (Kamann et al. 2014)[53]. In the discs of larger galaxies, IMBHs are found as ultra-luminous X-ray sources (e.g. Farrell et al. 2009)[33].

Lützgendorf et al. (2013)[62] studied a sample of 14 galactic GCs finding a strong correlation between the mass of the IMBH and velocity dispersion of the host GC. The correlation

can be expressed by the standard M_{SMBH}–σ equation

$$\log_{10}(M_{IMBH}) = \alpha_{\sigma} + \beta_{\sigma} \log_{10}[\sigma/(200)], \qquad (1.1.7)$$

with the values $\alpha_{\sigma} = 6.51 \pm 1.94$ and $\beta_{\sigma} = 2.34 \pm 1.63$. This scaling relation is similar to relationships found between the mass of SMBHs and the velocity dispersion of the host galaxy. However, the relationship for IMBHs is shallower. The authors find a correlation between the mass of the IMBH and the total mass of the GC, as well as a correlation between the mass of the IMBH and the total luminosity of the GC. These two scaling relations are also shallower versions of ones found for large galaxies hosting SMBHs.

IMBHs have also been sought in lower mass galaxies. Peterson et al. (2005)[77] studied the dwarf Seyfert galaxy NGC 4395 and constrained the mass of the central black hole to be $(3.5 \pm 1.1) \times 10^5 \, M_{\odot}$. Valencia et al. (2012)[96] investigated the starburst/Seyfert composite galaxy IRAS 01072+4954 using *HST* and 2MASS data. The authors present evidence for the presence of an IMBH of mass $< 10^5 \, M_{\odot}$ by using the SMBH scaling relations. These observations, along with others, may help to bridge the gap between SMBHs and IMBHs (or determine if it is a continuum).

1.1.2 Nuclear Star Clusters

In the early photographic survey of early-type galaxies in the Virgo cluster, Binggeli et al. (1985)[4] found that many of the dwarf elliptical galaxies show unresolved nucleation. Over the last decade, *HST* imaging studies have led to the discovery of large, compact stellar clusters that sit in the centre of most low to intermediate mass galaxies. Côté et al. (2006)[20] revisited the Virgo cluster using *HST* data and found that $66\% \leq f_n \leq 82\%$, low to intermediate luminosity, early-type galaxies were nucleated. This was higher than the fraction for similar luminosity elliptical obtained by Binggeli et al. (1985)[4], because of a

surface brightness selection effect (Côté et al. 2006)[20].

These nuclear star clusters (NSCs) have since been found in a wide variety of Hubble types, suggesting that the link between their formation and the evolution of their host galaxy is complex (Böker et al. 2010)[10]. Böker et al. (2002)[11] found that ~ 75 per cent of their sample of 77 face-on late-type (Scd-Sm) galaxies contained NSCs. Carollo et al. (1997)[16] studied earlier-type (Sa-Sc) spirals and showed that ~ 50 per cent contained a NSC. However, in more luminous galaxies, brighter than $M_B \simeq -20.5$, NSCs are less common (Côté et al. 2006; Grant et al. 2005)[20,46]. NSCs are much more luminous than GCs, with typical absolute I-band magnitudes of -14 to -10 (Böker et al. 2002; Côté et al. 2006)[11,20]. They are also extremely massive and compact, with a mass range of $10^6 - 10^7\,M_\odot$ and a typical half-light radius within the range of $2-5\,\mathrm{pc}$[11,20,39,104]

Because NSCs sit at the bottom of their host galaxies' potential well, they are subject to different physical conditions than the rest of the galaxy. These conditions can lead to various distinctive phenomena: active galactic nuclei (AGN), central starbursts and extreme stellar densities. The scaling relationships discussed so far have been between SMBHs and their host galaxies, but now NSC scaling relationships relative to their host galaxy will be discussed. In some cases NSCs and SMBHs are considered as a single class of objects (CMOs) (Ferrarese et al. 2006)[35]. A recent example of this is Scott et al. (2013)[85], in which the authors investigate the scaling relationship between the mass of CMOs and the velocity dispersion of their host galaxy. They find that the strongest correlation is between the mass of the NSC and the host galaxy's velocity dispersion. This correlation is shallower than the relation defined by SMBHs and is given by

$$\log_{10} M_{NSC} = (2.11 \pm 0.31)\log_{10}(\sigma/54) + (6.63 \pm 0.09). \qquad (1.1.8)$$

However, Erwin & Gadotti (2012)[32] highlighted some of the problems to be considered when examining these relationships. First, the masses of NSCs are based on the measured

velocity dispersion of the NSC which can be indistinguishable from that of the surrounding bulge. Secondly, that NSCs can be found in galaxies with no detectable bulge at all (Seth at al. 2006)[92]. Finally, it is difficult to see how one should discriminate between the contribution of velocity dispersion from the bulge and that of the whole galaxy. They go on to investigate the relationship between NCSs properties of their host galaxy. The authors compare the NSC to the SMBH mass, bulge mass and total stellar mass. Erwin & Gadotti (2012)[32] found that NSCs scale more closely with total stellar mass, than they do with mass of the bulge. This has led to the incarnation of a single class of central massive objects (CMOs). We see that in a specific galaxy the type of CMO that resides in its nucleus is dependent on the mass of the host galaxy. Galaxies with a mass of $\lesssim 10^7 \, \mathrm{M_\odot}$ generally host a NSC and more massive galaxies predominantly host SMBHs. These connections between SMBHs and NSCs leave many questions open. For example, what happens in galaxies like the Milky Way that host both a NSC and a SMBH?

Another question, that is yet to be conclusively answered, is how do NSCs form? The suggested scenarios can generally be categorized into two classes: migratory formation scenarios in which dense clusters form elsewhere in the galaxy then fall into the centre due to dynamical friction (Chandrasekhar 1943)[17] and in-situ cluster build up driven by gas infall and subsequent star formation (possibly episodic).

Capuzzo-Dolcetta & Miocchi (2008)[15] investigated the migratory formation scenario and found that it is a viable formation scenario under certain initial conditions. Using self-consistent N-body simulations of four GCs migrating to the galactic centre, Capuzzo-Dolcetta & Miocchi (2008)[15] found that the projected density profile and central kinematics closely resemble the resolved galactic nucleus. Andersen et al. (2008)[1] studied the bulge-less galaxy NGC 2139. They find a young, cluster that sits 320 pc from the galactic centre. The authors show that the galaxy is not in dynamic equilibrium and propose that the cluster may come to rest at the galactic centre within a few 100 Myr, becoming a NSC. Hartmann

et al. (2011)[50] also investigated this formation process by comparing observations and dynamical models of the NSCs in both NGC 4244 and M33, to an extensive set of *N*-body simulations. These simulations form a NSC by letting GCs sink to their centre. The authors show that the process could produce a wide variety of the observed properties of NSCs such as the density distribution, structural scaling relations and even rapid rotation. However, the underlying kinematics of the NSCs did not match with observations as the second order kinematic moment V$_{rms}$ was peaked at the centre, contrary to the observations.

On the other hand, infall of molecular gas into the inner few parsecs does occur. A variety of mechanisms have been proposed for the driving of gas to the central region, including magneto-rotational instability (Milosavljević 2004)[74] and the action of instabilities (Shlosman & Begelman 1989)[94]. This infall would possibly lead to NSC formation and thus supports the in-situ formation scenario. Further work has been performed on this scenario by Emsellem et al. (2008) and Milosavljević (2004)[31,74]. A possible driving force in moving gas to the central region can be found when one considers the impact of the bar's potential on the motions of the gas. Sakamoto et al. (1999), Sheth et al. (2005), Wang et al. (2012)[80,93,105] and others all find that barred galaxies harbour more molecular gas and have increased star-formation in their central regions. This central increase in gas density could also explain the origin of the gas needed for the in situ-formation hypothesis. Although, this does not completely solve the issue because NSCs are found in both early- and late-types, many of which do not contain bars.

Multi-component nature

Assuming that NSCs consist of a single—often spheroidal—component is not unreasonable for some systems. However, some NSCs display signs that they also host a separate component that is not well represented by a single spheroid. This has been shown by Schinnerer et al. (2003), Rossa et al. (2006), Walcher et al. (2005), Walcher et al. (2006), Seth

et al. (2006), Seth et al. (2010) and Lyubenova et al. (2013)[64,79,82,90,92,103,104]. Seth et al. (2006)[92] looked a number of edge-on galaxies that contained NSCs and found evidence that some host multiple components. These components are very compact with scale lengths and half-light radii of 2–30 pc. They define two separate components, the nuclear cluster disc (NCD) and the nuclear cluster spheroid (NCS). Not only do these NSCs have two distinct components, but the NCDs are made up of younger stars than its spheroidal counterpart. Seth et al. (2006)[92] found the discs to be 0.3–0.6 mag bluer in F606W & F814W than the reddest parts of the spheroids. This colour difference can be simply interpreted as a difference in the stellar age, the discs having a stellar population with ages $\simeq 1$ Gyr. However, it is also worth noting that as these two components overlap, one would expect the observed difference to be smaller than that of the actual populations.

1.1.3 NGC 4244

Fig. 1.2 SDSS G, R and I band composite image of NGC 4244. *Image credit: David W. Hogg, Michael R. Blanton and the Sloan Digital Sky Survey Collaboration.*

One of the galaxies studied by Seth et al. (2006)[92] containing a multi-component NSC

was NGC 4244. The authors show that NGC 4244 is best fit by the combination of a spheroid and a disc. The authors also fitted a spheroid and ring, however, this proved be an inferior fit to the NSC.

Hartmann et al. (2011)[50] investigated the role of star cluster merging on the formation of NSCs. In their study they produced Jeans Anisotropic Multi-Gaussian Expansion (JAM) dynamical models of both NGC 4244 and M33. These models produced a negative vertical anisotropy ($\beta_z = 1 - \sigma_z^2/\sigma_R^2$) for the NSC of NGC 4244. However, in N-body simulations used to form NSCs, from merging star clusters, the remnant contained a centrally peaked V_{rms} distribution, contrary to the observations. To remove this effect, the authors show that the NSC requires at least 50 per cent of the mass accreted to be gas. However, the negative vertical anisotropy can not be obtained from the accretion of gas. To achieve $\beta_z < 0$ their simulations required the merger of star clusters on highly inclined (polar) orbits, containing a total of at least 10 per cent of the total NSC mass. This vertical anisotropy may be a product of the multi-component modelling technique.

De Lorenzi et al. (2013)[24] dynamically modelled the NSC of NGC 4244 using the χ^2-made-to-measure code NMAGIC, with two separate components. Similar to Seth et al. (2006)[92], De Lorenzi et al. (2013)[24] used the combination of a spheroidal component and a disc component. The models of De Lorenzi et al. (2013)[24] also displayed a negative vertical anisotropy. However, it has been postulated that hosting an IMBH can decrease the vertical anisotropy of the model by scattering box orbits (Merritt & Quinlan 1998)[72]. The upper limit on the central black hole mass was then constrained by including a central IMBH of mass $0 \leq M_{IMBH} \leq 3.0 \times 10^5 \, \mathrm{M_\odot}$. While this does increase the vertical anisotropy, it still remains negative within the effective radius of the NSC. Therefore, the NSC must be vertically anisotropic even if an IMBH were present. The vertical anisotropy can be removed in N-body simulations by the accretion of a star cluster. The accretion of a star cluster containing just 13 per cent of the mass of the NSC can remove this vertical anisotropy.

Because Cappellari (2008)[13] found that a decrease in inclination leads to an increase in vertical anisotropy, De Lorenzi et al. (2013)[24] also measured the vertical anisotropy for models at different inclinations. They show that the vertical anisotropy does increase, yet remains negative. Therefore, the vertical anisotropy is not a projection effect and is an intrinsic feature of the NSC. The authors also found the mass of the NSC to be $M_{NSC} = 1.6^{+0.5}_{-0.2} \times 10^9 \, M_\odot$ within 42.4 pc and the mass of just the bluer disc component to be $3.6 \times 10^5 \lesssim M_{NCD} \lesssim 14.4 \times 10^5 \, M_\odot$. NGC 4244 lies above the mass scaling relations proposed by Scott & Graham (2013)[85]. This thesis addresses the question: is NGC 4244 better modelled by a single spheroidal component, or by the multi-component models of De Lorenzi et al. (2013)[24]?

1.1.4 Messier 33

Messier 33 (M33) is a spiral galaxy in the Local Group, at a distance of 809 ± 30 kpc (Scowcroft et al. 2009)[86]. Early work on the nucleus of M33 by Kormendy & McClure (1993)[57] showed that it was very dense, with a central density of $\rho_0 \gtrsim 5 \times 10^5 \, M_\odot \, \mathrm{pc}^{-3}$. Kormendy & McClure (1993)[57] also classify M33 as a high-luminosity galaxy because of its low mass-to-light ratio of $M/L_V \gtrsim 0.4$. The authors also derive a strict mass limit for the central black hole of $5 \times 10^4 \, M_\odot$. More recently, Lauer et al. 1998[59] studied the nucleus of M33, finding a central density of $\rho_0 > 2 \times 10^6 \, M_\odot \, \mathrm{pc}^{-3}$. Ground based observations of M33 show no evidence for a central rise in velocity dispersion, which would indicate the presence of a SMBH (Kormendy & McClure 1993; Lauer et al. 1998)[57,59].

Merritt et al. 2001[71] used the *HST* to observe M33. They confirmed that neither the mean velocity nor the mean velocity dispersion rise in the nucleus of M33. They then continued to construct spherical two-integral models of the nucleus of M33. The authors found that the best fitting black hole mass was zero and the upper limit was $3 \times 10^3 \, M_\odot$, which puts M33 off the $M_{SMBH}-\sigma$ relation of Ferrarese & Merritt (2000)[36]. Similarly Gebhardt et al.

Fig. 1.3 2MASS J, H and Ks band composite image of Messier 33 (Jarrett et al. 2003)[51].

(2001)[38] used observations of M33 from the HST to determine the mass of the central black hole. They also found no central rise in the velocity or velocity dispersion. By constructing three-component orbit-based spheroidal models (Schwarzschild 1979), the authors find that the best fitting black hole mass for M33 is zero and that the upper limit on the black hole mass is $1.5 \times 10^3 \, M_\odot$. This upper limit is even lower than that of Merritt et al. (2001)[71]. Gebhardt et al. (2001)[38] also confirmed that this result is not a projection effect by constructing models at different inclinations, from face-on, to edge-on. However, they found that none of their models could properly match their observed fourth order Gauss-Hermite moment h_4 for the inner few bins (~ 0.1 arcsec). They confirm that this discrepancy is not due to an artifact of either the data or the data analysis. Therefore, it is a real feature that they are unable to reproduce in their models.

During the study by Hartmann et al. (2011)[50], the authors found no evidence for non-

axisymmetry in the NSC of M33. They also find that its position angle (PA) is consistent with that of the main disc and is elliptical with a vertical flattening of $q = 0.7$, similar to the NSCs in edge-on spirals (Seth et al. 2006)[92]. Hartmann et al. (2011)[50] also show that the density, size and ellipticity of M33 can all be recreated by simulations in which young star clusters accrete onto a bare NCD. However, the problem of the V$_{rms}$ remains.

1.1.5 The distribution function

To model a stellar system, we need an expression that defines how the stars are distributed. This distribution is a product of the motions of stars within a stellar population. One problem when looking at the motions of star is the effect of other bodies. When looking at GCs containing $\sim 10^5$ stars these interactions can play a substantial role on the overall evolution of the cluster. However, for galaxies comprised of $\sim 10^{11}$ stars these stellar encounters are largely unimportant. In these cases where the individual stellar interactions only play a small role, one may make the assumption that the system is *collisionless*. In a *collisionless system*, the orbit of a particle is only affected by the mean potential generated by all other particles. For a large number of stars moving under the influence of a smooth potential $\phi(\mathbf{x},t)$, at any time t, a full description of the collisionless system is given by a specified number of stars, within the six-dimensional phase-space volume $\mathrm{d}^3\mathbf{x}\mathrm{d}^3\mathbf{v}$. These stars follow the *distribution function* (DF),

$$f(\mathbf{x},\mathbf{v},t), \tag{1.1.9}$$

which gives the probability of a star, at time t, having phase-space coordinates within the given range. Assuming that all the stars are the same, therefore, the DF gives the probability of any star $1,\ldots,N$, at time t, having phase-space coordinates within the given range $(x,x+\mathrm{d}x)$. Let $\mathbf{w} = (\mathbf{x},\mathbf{v})$ be the usual Cartesian coordinates, then for a given volume $\mathscr{V}$, the

probability of finding a star within $\mathscr{V}$ is given by

$$P = \int_{\mathscr{V}} f(\boldsymbol{w}) \, \mathrm{d}^6 \boldsymbol{w}. \tag{1.1.10}$$

In many applications it is often useful to define the DF in an arbitrary coordinate system $\boldsymbol{W}$; then the corresponding DF is $F(\boldsymbol{W})$. If $\mathscr{V}$ is small enough, f and F will be approximately constant, thus we can take them outside of the integral in equation (1.1.6) giving

$$P = f(\boldsymbol{w}) \int_{\mathscr{V}} \mathrm{d}^6 \boldsymbol{w} = F(\boldsymbol{W}) \int_{\mathscr{V}} \mathrm{d}^6 \boldsymbol{W}. \tag{1.1.11}$$

If the coordinate system we choose for $\boldsymbol{W}$ is canonical, since the phase-space volume is the same in any canonical coordinate system (Binney & Tremaine 2008)[7], we have that

$$\int_{\mathscr{V}} \mathrm{d}^6 \boldsymbol{w} = \int_{\mathscr{V}} \mathrm{d}^6 \boldsymbol{W}. \tag{1.1.12}$$

Therefore, the DF has the same value at any point in phase-space, in any given canonical coordinate system. Thus, we can treat $\boldsymbol{w} = (\boldsymbol{x}, \boldsymbol{v})$ as any arbitrary canonical coordinate system (Binney & Tremaine 2008)[7].

As a star moves through phase-space the probability of finding it at a given point in phase-space changes with respect to time. However, the total probability of finding the particle in the entire volume must remain constant. This constraint can be thought of as the conservation of mass in fluid flow, which is described by the continuity equation. The analogous equation for the conservation of probability in phase-space is given by

$$\frac{\partial f}{\partial t} + \frac{\partial}{\partial \boldsymbol{w}} \cdot (f \dot{\boldsymbol{w}}) = 0. \tag{1.1.13}$$

15

The Hamilton equations are given by

$$\dot{\boldsymbol{q}} = \frac{\partial H}{\partial \boldsymbol{p}}, \tag{1.1.14a}$$

$$\dot{\boldsymbol{p}} = \frac{\partial H}{\partial \boldsymbol{q}}. \tag{1.1.14b}$$

Substituting the Hamilton equations into the second term of equation (1.1.9) and using the chain rule, yields

$$\frac{\partial}{\partial \boldsymbol{q}} \cdot (f\dot{\boldsymbol{q}}) + \frac{\partial}{\partial \boldsymbol{p}} \cdot (f\dot{\boldsymbol{p}}) = \frac{\partial}{\partial \boldsymbol{q}} \cdot \left(f\frac{\partial H}{\partial \boldsymbol{p}} \right) - \frac{\partial}{\partial \boldsymbol{p}} \cdot \left(f\frac{\partial H}{\partial \boldsymbol{q}} \right), \tag{1.1.15a}$$

$$= \frac{\partial f}{\partial \boldsymbol{q}} \cdot \frac{\partial H}{\partial \boldsymbol{p}} - \frac{\partial f}{\partial \boldsymbol{p}} \cdot \frac{\partial H}{\partial \boldsymbol{q}}, \tag{1.1.15b}$$

$$= \dot{\boldsymbol{q}} \cdot \frac{\partial f}{\partial \boldsymbol{q}} + \dot{\boldsymbol{p}}\frac{\partial f}{\partial \boldsymbol{p}}. \tag{1.1.15c}$$

By substituting equation (1.1.11c) back into equation (1.1.9), we obtain the collisionless Boltzmann equation

$$\frac{\partial f}{\partial t} + \dot{\boldsymbol{q}} \cdot \frac{\partial f}{\partial \boldsymbol{q}} + \dot{\boldsymbol{p}}\frac{\partial f}{\partial \boldsymbol{p}} = 0. \tag{1.1.16}$$

The Jeans equations

As the DF is a function of seven variables, the complete solution of the collisionless Boltzmann equation is often extremely complex. However, information can still be gained by taking moments of the collisionless Boltzmann equation. Jeans (1915)[52] derived three equations (first derived by Maxwell), analogous to the Euler equations for fluid flow, to describe the motion of a collection of stars within a gravitational field. Assuming that almost all

orbits are regular with non-resonant frequencies these equations are given by

$$\frac{\partial v}{\partial t} + \sum_i \frac{\partial (v \bar{v}_i)}{\partial x_i} = 0, \tag{1.1.17a}$$

$$\frac{\partial (v \bar{v}_j)}{\partial t} + v \frac{\partial \Phi}{\partial x_j} + \sum_i \frac{\partial (v \overline{v_i v_j})}{\partial x_i} = 0, \tag{1.1.17b}$$

$$\frac{\partial (v \bar{v}_j)}{\partial t} + v \bar{v}_i \frac{\partial \bar{v}_j}{\partial x_i} = -v \frac{\partial \Phi}{\partial x_j} - \frac{\partial (v \sigma_{ij}^2)}{\partial x_i}. \tag{1.1.17c}$$

Here $v(\boldsymbol{x})$ is the spatial density of stars given by

$$v(\boldsymbol{x}) \equiv \int f \, \mathrm{d}^3 \boldsymbol{v}, \tag{1.1.18}$$

the mean stellar velocity is given by

$$\bar{v}_i \equiv \frac{1}{v(\boldsymbol{x})} \int f v_i \, \mathrm{d}^3 \boldsymbol{v}, \tag{1.1.19}$$

with

$$\overline{v_i v_j} = \frac{1}{v(\boldsymbol{x})} \int v_i v_j f \, \mathrm{d}^3 \boldsymbol{v}, \tag{1.1.20}$$

and

$$\sigma_{ij}^2 = \overline{(v_i - \bar{v}_i)(v_j - \bar{v}_j)}. \tag{1.1.21}$$

Here, the stress tensor $v \sigma_{ij}^2$ describes the anisotropic pressure. When solving the Jeans equations, the stress tensor is problematic. In a fluid the form of σ_{ij}^2 is given by the state of the fluid, however, in a stellar system we lack an accurate analogue for this. Therefore, in order to progress using the Jeans equations for stellar systems, some assumptions must be made.

Solving the Jeans equations for a spherical density

In order to solve the Jeans equations we must find an expression for the velocity-dispersion tensor $\boldsymbol{\sigma}$. A simple expression for $\boldsymbol{\sigma}$ can be found if we assume that the DF depends only on the Hamiltonian $H = \frac{1}{2}v^2 + \Phi(\boldsymbol{x})$. For this case the system of particles uniformly explores the energy surface in phase-space. In such a case the velocity dispersion tensor is isotropic, thus σ_{ij}^2 is diagonal, i.e.

$$\sigma_{ij}^2 = \overline{v_i v_j} = \sigma^2 \delta_{ij}, \tag{1.1.22}$$

where

$$\sigma^2(\boldsymbol{x}) = \frac{4\pi}{3v(\boldsymbol{x})} \int_0^\infty v^4 f\left(\frac{1}{2}v^2 + \Phi\right) \mathrm{d}v. \tag{1.1.23}$$

For a more general expression, we can assume that the DF is spherical and depends on the Hamiltonian $H = \frac{1}{2}(v_r^2 + v_t^2) + \Phi(r)$ and the angular momentum vector $L = rv_t$. Here v_r and $\boldsymbol{v_t}$ are the components of $\boldsymbol{v}$ parallel and perpendicular to the radial direction. For this case the velocity-dispersion is diagonal with diagonal components given by

$$\sigma_r^2 \equiv \overline{v_r^2} = \frac{2\pi}{v} \int_{-\infty}^\infty v_r^2 \, \mathrm{d}v_r \int_0^\infty v_t f\left[\frac{1}{2}(v_r^2 + v_t^2) + \Phi, rv_t\right] \mathrm{d}v_t, \tag{1.1.24a}$$

$$\sigma_\theta^2 \equiv \overline{v_\theta^2} = \frac{\pi}{v} \int_0^\infty v_t^3 \, \mathrm{d}v_t \int_{-\infty}^\infty v_r f\left[\frac{1}{2}(v_r^2 + v_t^2) + \Phi, rv_t\right] \mathrm{d}v_r, \tag{1.1.24b}$$

$$\sigma_\phi^2 = \sigma_\theta^2. \tag{1.1.24c}$$

Solving the Jeans equations for an axisymmetric density

It is not always reasonable to assume the system is spherically symmetric. For an expression of $\boldsymbol{\sigma}$ which is instead axisymmetric we must consider a DF that depends on the Hamiltonian and the angular momentum about the symmetry axis $L_z = Rv_\phi$. For this case the velocity-

dispersion is diagonal with diagonal components given by

$$\sigma_R^2 = \overline{v_R^2} = \frac{1}{v} \int v_R^2 \, \mathrm{d}v_R \int \mathrm{d}v_z \int f \left[\frac{1}{2}(v_R^2 + v_z^2 + v_\phi^2) + \Phi, Rv_\phi \right] \mathrm{d}v_\phi, \tag{1.1.25a}$$

$$\sigma_z^2 = \sigma_R^2, \tag{1.1.25b}$$

$$\sigma_\phi^2 = \frac{1}{v} \int (v_\phi - \bar{v}_\phi)^2 \, \mathrm{d}v_\phi \int \mathrm{d}v_R \int f \left[\frac{1}{2}(v_R^2 + v_z^2 + v_\phi^2) + \Phi, Rv_\phi \right] \mathrm{d}v_z. \tag{1.1.25c}$$

For stars in the solar neighbourhood the radial velocity dispersion and the vertical velocity dispersion are measured to not be the same, i.e. equations (1.1.20c) and (1.1.21b) do not hold (Binney & Tremaine 1987)[6]. Therefore, there must be a third isolating integral, which is generally unknown.

1.1.6 Modelling Techniques

There are numerous methods for constructing models of stellar systems, which can be classified into the following: distribution function (DF) based, moment-based, orbit-based and particle-based. We will now briefly look at how these different methods work.

1. DF-based methods solve directly for the DF and usually require all the integrals of motion to be known explicitly, which is often not the case. These include methods that fit observables to simple models with analytic DFs such as disc or King models. Merritt & Tremblay (1994)[73] used one of these methods to determine the density profiles near the centre of the Coma galaxy cluster and M15. They also discuss some of the problems with DF-based methods, the most significant is the choice of analytic DF. The choice of an analytic DF function requires the properties of the galaxy to be properly distinguished and a poorly chosen DF can cause a large bias on the model. A further problem with a DF-based approach is that generally the population has to be assumed axisymmetric. However, they lose generality when the DF depends on a third integral.

2. Moment-based methods find solutions to the Jeans equations or collisionless Boltzmann equation to minimize χ^2. These methods generally use one or two isolating integrals, however, some use a third integral but assumptions are made on its form. Binney & Mamon (1982)[5] used a method of this type to form spherical models of M87, for comparison with the models constructed by Duncan & Wheeler (1980)[29]. Binney & Mamon (1982)[5] demonstrate the reliability of the method by testing their algorithm on data generated from model galaxies of different brightness profiles and anisotropies. These methods have since been applied to axisymmetric models of elliptical galaxies (Binney et al. 1990; Magorrian & Binney 1994; van der Marel et al. 1994)[8,66,100]. More recently, Cappellari (2008)[13] generalized this technique in order to incorporate the multi-Gaussian expansion (MGE) technique for parametrising the galaxies photometry. These Jeans Anisotropic MGE (JAM) models have since been used for modelling galaxies and clusters (Seth et al. 2010; Hartmann et al. 2011; Emsellem 2013)[30,50,90]. However, a drawback is that these algorithms do not guarantee a positive-definite DF with the required kinematics (Syer & Tremaine 1996)[95].

3. Orbit-based methods (Schwarzschild 1979; Schwarzschild 1993)[83,84] compute the density distribution of a large library of orbits in a fixed potential, allowing three isolating integrals. The orbits are then weighted such that the system reproduces the desired final state for the system. These methods do not require the integrals of motion to be known explicitly. Orbit-based methods have been used for modelling a plethora of different stellar structures. In general orbit-based methods require large amounts of computing time and often require symmetry assumptions to be made. However, this is not always the case and triaxial orbit-based models have been constructed (van den Bosch et al. 2008; Vasiliev 2013)[98,102].

4. Particle-based methods (Syer & Tremaine 1996)[95] integrate over a particle system while slowly changing the weights of individual particles. This integration and weight-

ing is continued until some set of observed values are matched for the observables of the system. These methods complement orbit-based methods but do not require the user to store a large library of orbits for the system, only a list of updated particle weights. This method can accommodate three isolating integrals in their DF. Such models have been used for galaxies and star clusters (De Lorenzi et al. 2008; De Lorenzi 2009; Long & Mao 2012; Morganti & Gerhard 2012; De Lorenzi et al. 2013)[22–24,60,75]

Chapter 2

Observations of nuclear star clusters

2.1 Observational data for NGC 4244 and M33

The observational data for NGC 4244 and M33 that were used for the models in this thesis were similar to those described in Seth et al (2010)[90] for NGC 404. They consisted of a combination of different data from different instruments including: near-infrared (NIR) Integral Field Unit spectroscopy from Gemini's Near-Infrared Integral Field Spectrometer (NIFS) (These observations are part of the ongoing survey of nearby NSCs led by Seth et al. (2009)[88], optical long-slit spectra from the Multiple Mirror Telescope (MMT) and *HST* imaging data from ultraviolet (UV) to NIR. Some observational information is given in tables 2.1 & 2.2. The kinematics, from the Gemini NIFS data, consist of velocity, velocity dispersion and the higher order Gauss-Hermite moments h_3 and h_4 (Gerhard 1993)[41].

Reducing the observational data for M33 proved more challenging than for NGC 4244. The most pressing issue was the presence of bright, young, resolved stars forming large peaks or deficits in the kinematic data. It was necessary to disentangle the kinematics of these individual stars from the underlying diffuse light, Seth started by finding all the individual stars that were at least 7 pixels from the centre and contributed at least 20 percent of the light in an individual pixel; a total of 28 stars were identified. These stars' kinematics

Distance [Mpc]	4.370 ± 0.03^a
distance modulus $[m - M]$	28.20 ± 0.03^a
pc asec^{-1}	21.19
Total magnitude [V band]	-18.63 ± 0.16^b
[K band]	-24.1 ± 0.05^c
Heliocentric velocity	244 ± 1^d
Inclination [degrees]	90^e
Position Angle [degrees]	47.2^e
Flattening $[q]$	0.81^e

Table 2.1 Properties of NGC 4244.
[a] Tip of the Red Giant Branch (TRGB) measurement from Seth et al. (2005)[91]
[b] absolute magnitude in the visual band (551 nm) measurement from de Vaucouleurs et al. (1991)[27]
[c] absolute magnitude in the K band (2.2 μm) measurement from Jarrett et al. (2003)[51]
[d] measurement from Olling (1996)[76]
[e] measurement from from Seth et al. (2005)[91]

Distance [Mpc]	0.809 ± 0.06^a
distance modulus $[m - M]$	24.54 ± 0.06^a
pc asec^{-1}	3.92
Total magnitude [V band]	-19.41 ± 0.04^b
[K band]	-20.44 ± 0.04^c
Heliocentric velocity [km s^{-1}]	-179 ± 3^d
Inclination [degrees]	56^e
Position Angle [degrees]	38^f
Flattening $[q]$	0.85

Table 2.2 Properties of M33.
[a] Tip of the Red Giant Branch (TRGB) measurement from McConnachie et al. (2005)[69]
[b] absolute magnitude in the visual band (551 nm) measurement from de Vaucouleurs et al. (1991)[27]
[c] absolute magnitude in the K band (2.2 μm) measurement from Jarrett et al. (2003)[51]
[d] measurement from de Vaucouleurs et al. (1991)[27]
[e] measurement from Zaritsky et al. (1989)[106]
[f] measurement from Corbelli et al. (2010)[19]

were then fitted to a single pixel containing the largest fraction of the light from this star.

This stellar fit was deemed acceptable only if all of the following conditions were met:

1. the fit yields a low dispersion (<10 km/s)

2. a reasonable amount of light has been fitted, subject to a radius of 3-5 pixels from the object.

Of the 28 stars, ten single-pixel spectra are not well fit by a single star and the affected regions around these stars have been flagged to be avoided by the model. For stars with good fits, the best fitting star spectrum was then fit as a "sky background" from 3 pixel radius apertures around each star to determine the underlying kinematics.

For smoother kinematics it is common to *symmetrize* the observational data. This can be thought of as 'folding' the kinematic maps at the position angle and comparing each pixel that are now folded together. In order to do this accurately, we must first know the position angle (PA). For NGC 4244 the PA is readily given by Seth et al. (2005)[91]. However, the PA of M33 is more disputed with a range of values from 0 to 50 (de Vaucouleurs 1959; Sandage & Humphreys 1980; Zaritsky et al. 1989; Corbelli et al. 2010)[19,26,81,106]. For the NIFS data of M33's NSC we find a best fit PA of 33-39 degrees, therefore, we take the PA of 38 degrees from Corbelli et al. (2010)[19]. The new symmetrized kinematics for each pixel are then given by the following equations,

$$v_{sym} = \pm(v_1 - v_2)/2, \qquad (2.1.1a)$$

$$\sigma_{sym} = (\sigma_1 + \sigma_2)/2, \qquad (2.1.1b)$$

$$h_{3,sym} = \pm(h_{3,1} - h_{3,2})/2, \qquad (2.1.1c)$$

$$h_{4,sym} = (h_{4,1} + h_{4,2})/2, \qquad (2.1.1d)$$

where the sign of v_{sym} and $h_{3,sym}$ depend on which side of the map under are consideration. This can smooth the kinematic maps, however, if the original map has large peaks or deficits, this process doubles the amount of these problematic regions. Therefore, the map that is going to be symmetrized needs to be relatively smooth to begin with. Otherwise, one must

note every pair of pixels where their absolute values are very different and implement some process to determine which value is correct, which introduces a selection bias. We chose to ignore bins in which the absolute values of the kinematics were different by one or more orders of magnitude.

2.2 Fitting

The fitting of analytical functions to light distributions is the first step in dynamical modelling galaxies. By fitting an analytical function one can better understand the structure of the object but a bias is introduced by the functional form. First we must determine the shape of the object. Initally NSCs were thought to be similar to elliptical galaxies, therefore, the fitting functions for elliptical galaxies were often used to model the distribution of light in a NSC. For elliptical galaxies one of the early functional forms was the de Vaucouleurs ($r^{1/4}$) law (de Vaucouleurs 1948)[25], given by

$$I(r) = I_e \exp \left\{ -7.67 \left[\left(\frac{r}{r_e} \right)^{1/4} - 1 \right] \right\}, \qquad (2.2.1)$$

where $I(r)$ is the intensity at radius r and I_e is the intensity at the effective radius r_e, which encloses half of the total light. This is an empirical law which has been used to fit the surface brightness profiles of many galaxies and can even be used to fit some classical bulges. A generalisation of this law was proposed by Sérsic (1963)[87] by defining

$$I(r) = I_e \exp \left\{ -b_n \left[\left(\frac{r}{r_e} \right)^{1/n} - 1 \right] \right\}, \qquad (2.2.2)$$

where, b_n is used to describe the shape and n is the Sérsic index (which is positive and real). The Sérsic index n allows the profile to be very versatile, for example $1.5 < n < 20$ can describe elliptical galaxies while $1 < n < 2$ can be used to describe pseudo-bulges. For

$n = 4$ the de Vaucouleurs law is recovered. Sérsic profiles are often used to fit bulges[44], but can also be used to fit some elliptical galaxies well and is used commonly to fit NSCs (for review of the properties of the Sérsic profile, see Ciotti & Bertin 1999)[18].

Because it is possible that NSCs form out of the merging of globular clusters, it is reasonable to assume that NSCs also follow the same light distribution. King (1978)[54] proposed a distribution function for globular clusters by treating them as truncated isothermal spheres, defining the King profile

$$\Sigma(r) = \Sigma_0 \left[\frac{1}{\sqrt{1 + (r/r_{core})^2}} - \frac{1}{\sqrt{1 + (r_{tidal}/r_{core})^2}} \right], \qquad (2.2.3)$$

where $\Sigma(r)$ is the projected surface brightness at radius r, Σ_0 is the central surface brightness, r_{core} is the core radius at which the brightness is half the central brightness and r_{tidal} is the tidal radius at which point the brightness vanishes. The King profile has been used to fit many globular clusters (Harris et al. 1991; McLaughlin 1995; Kissler-Patig & Gebhardt 1998; Rhode & Zepf 2001; Harris 2009)[48,49,55,70,78] and some NSCs (Böker et al. 2004; Seth et al. 2006)[12,92]. However, most NSCs are not spheres but spheroidals with some flattening coefficient q, which is given by the axial ratio (minor/major). If we account for this the King profile becomes

$$\Sigma(R) = \Sigma_0 \left[\frac{1}{\sqrt{1 + (R/r_{core})^2}} - \frac{1}{\sqrt{1 + (r_{tidal}/r_{core})^2}} \right], \qquad (2.2.4)$$

$$\text{with } R = \sqrt{x^2 + (z/q)^2}. \qquad (2.2.5)$$

An example of a galaxy with a NSC that is best fit by a single component King model is the SBc galaxy NGC 4144 (Seth et al. 2006)[92].

Numerous NSCs are comprised of not just a spheroidal component but also a disk com-

ponent (Seth et al. 2006)[92]. This requires models with two different components, a nuclear cluster spheroid (NCS) and a nuclear cluster disc (NCD), each having very different light distributions. For the NCS one can either use a Sérsic profile, or a King profile and for the second component one can either use a disc profile, or a ring profile. A simple disc profile can be expressed as

$$\Sigma(r) = \Sigma_0 \exp\left[\frac{-r}{r_e}\right]. \qquad (2.2.6)$$

A disc in combination with a Sérsic or King profile can fit the surface brightness of some NSCs well (for example NGC 4244; Seth et al. 2006)[92]. However, a King profile can also be used with a ring profile, which contributes a small amount of light in the centre but more light further out. An example of a ring profile from Seth et al. (2006)[92] can be expressed as follows,

$$\Sigma(x,z) = \begin{cases} 2\rho_0 \text{sech}^2\left(\frac{z}{z_0}\right)\left(\sqrt{r_{out}^2 - x^2} - \sqrt{r_{in}^2 - x^2}\right), & x < r_{in} \\ 2\rho_0 \text{sech}^2\left(\frac{z}{z_0}\right)\left(\sqrt{r_{out}^2 - x^2}\right), & r_{in} < x < r_{out} \\ 0, & \text{else.} \end{cases}$$

Various combinations of King, Sérsic, disc and ring can be used when modelling NSCs.

Chapter 3

Made-to-measure modelling

3.1 Classical made-to-measure modelling

This section follows the work of Syer & Tremaine (1996)[95] (hereafter ST96) and De Lorenzi et al. (2007)[21] (hereafter DL07). The made-to-measure (M2M) algorithm is designed to build a particle-based dynamical model of some target system. The algorithm adapts the system by changing the weights of the particles moving in the global potential, minimizing the differences between the model and the target's observables. These observables can be the density distribution and/or the line-of-sight kinematics. Any observable of a system can be characterized by a distribution function (DF) $f(z)$. These observables are defined as

$$Y_j = \int K_j(\boldsymbol{z}) f(\boldsymbol{z}) \mathrm{d}^6 z, \tag{3.1.1}$$

where K_j is a known kernel and $z = (r, v)$ are the phase-space coordinates. The equivalent observable of the particle model is given by the equation

$$y_j(t) = \sum_{i=1}^{N} w_i K_j[\boldsymbol{z}_i(t)], \tag{3.1.2}$$

where w_i are the weights and $\mathbf{z}_i$ are the phase-space coordinates of the particles. For the following, we set the weights to unity such that $w_i = 1$, for $i = 1,\dots,N$. Thus, the mass of each particle can be defined with respect to the total mass of the system simply as $m_i = w_i M/N$, where M is the total mass of the system. Given any set of observables Y_j, $j = 1,\dots,J$, we want to form a system of N particles orbiting in the system's potential, such that the observables of both systems converge to some defined χ^2. The most important part of the algorithm is defining how the weights of the particles are to change. The 'force-of-change' (FOC), which describes how the weights change, can be defined as

$$\frac{\mathrm{d}w_i(t)}{\mathrm{d}t} = -\varepsilon w_i(t) \sum_{j=1}^{J} \frac{K_j[\mathbf{z}_i(t)]}{Z_j} \Delta_j(t). \tag{3.1.3}$$

Here,

$$\Delta_j(t) = \frac{y_j(t)}{Y_j} - 1 \tag{3.1.4}$$

measures the difference between the observables of the target and the model, where ε is a small positive constant and the Z_j are all arbitrary constants. The dependence on w_i ensures that the FOC will never force a particle's weight to become negative. The dependence of the kernel K_j ensures that a mismatch in observable J only influences the weight of particle i if that particle would contribute to the observable j. The choice of Δ makes the algorithm closely related to Lucy's method (Lucy 1974)[61] which iteratively solves an integral equation for the distribution from observational data (see Box 3.1.1).

Due to the number of particles normally greatly exceeding the number of independent constraints, the solution of any set of differential equations of the form of the FOC, will be under-determined. This means that the weights of the particles can change and yet the observables of the model will remain constant. From ST96 a solution to this problem is to maximize the merit function

$$F = \mu S - \frac{1}{2}\chi, \tag{3.1.5}$$

29

with

$$\chi^2 = \sum_{j=1}^{J} \Delta_j^2 \tag{3.1.6}$$

and the entropy

$$S = -\sum_{i=1}^{N} w_i \log\left(\frac{w_i}{\hat{w}_i}\right) \tag{3.1.7}$$

is a profit function. $\{\hat{w}_i\}$ is a set of predetermined weights called the priors. Since

$$\mu \frac{\partial S}{\partial w_i} = -\mu \left[\log\left(\frac{w_i}{\hat{w}_i}\right) + 1 \right], \tag{3.1.8}$$

if a particle has weight $w_i < \hat{w}_i/e$ then the equation becomes positive, however, when $w_i > \hat{w}_i/e$, the equation becomes negative. Therefore, the entropy forces the particle weights to remain close to their corresponding prior in the set $\{\hat{w}_i/e\}$. From this we fix Z_j to Y_j and can now replace the equation for the FOC with

$$\frac{\mathrm{d}w_i(t)}{\mathrm{d}t} = \varepsilon w_i(t) \left[\mu \frac{\partial S}{\partial w_i}(t) - \sum_{j=1}^{J} \frac{K_j[z_i(t)]}{Y_j} \Delta_j(t) \right], \tag{3.1.9}$$

where μ is a constant governing how close the weights must remain to their priors. For large values of μ the weights $\{w_i\}$ will remain close to their priors $\{\hat{w}_i/e\}$ and for small values of μ the weights $\{w_i\}$ may deviate greatly from their priors. For the following we adopt $\hat{w}_i = w_0 = 1/N$, however, this is not necessary. Temporal fluctuations can often be a problem when dealing with a small number of particles N, therefore, ST96 & DL07 both adopt a temporal smoothing function by replacing Δ_j with $\tilde{\Delta}_j$, where

$$\tilde{\Delta}_j(t) = \alpha \int_{\tau=0}^{\tau=\infty} \Delta_j(t-\tau) \mathrm{e}^{-\alpha\tau} \, \mathrm{d}\tau, \tag{3.1.10}$$

and α is small and positive. $\tilde{\Delta}_j$ can also be thought of as the differential equation

$$\frac{d\tilde{\Delta}}{dt} = \alpha(\Delta - \tilde{\Delta}), \tag{3.1.11}$$

where $1/\alpha$ is the smoothing time. This equation helps to reduce the fluctuations in the model's observables. This also ensures that the particle weights change smoothly. Temporal smoothing can be thought of as effectively smearing the particle back along its orbit creating a number of 'ghost' particles. This modelling technique can be implemented to great effect for modelling density distributions (e.g. Bissantz et al. 2004)[9].

Box 3.1.1: Lucy's method

For fairly simple observed distributions, it can be difficult to determine the distribution function analytically. *Lucy's method* is an iterative numerical technique for finding the frequency function of a given quantity from an observed distribution. Lucy's equations are given as

$$\phi(x) = \int \psi(\xi) P(x|\xi) \, d\xi, \tag{3.1.12a}$$

$$\psi_{r+1}(\xi) = \psi_r(\xi) \int \frac{\tilde{\phi}(x)}{\phi_r(x)} P(x|\xi) \, dx, \tag{3.1.12b}$$

$$\tilde{\phi}(x) = \frac{1}{N} \sum_{n=1}^{N} \delta(x - x_n). \tag{3.1.12c}$$

Here $\phi(x)$ is the observed distribution, $\psi(\xi)$ is the frequency distribution of quantity ξ, $P(x|\xi)$ is the probability that x' will fall in the interval $(x, x + dx)$ and $\delta(x)$ is Dirac's delta function. For our purposes $\phi(x)$ is the observed density of the stellar system, $\psi(\xi)$ is the distribution function of mass ξ.

3.1.1 NMAGIC: a χ^2-made-to-measure modelling algorithm

This section describes the *N*-particle Made-to-measure AlGorithm mInimizing Chi squared (NMAGIC) code of DL07. This algorithm is a direct descendent of the ideas proposed by ST96 discussed above, with some new additions. The first important extension that was implemented by DL07 was the inclusion of a way to account for observational errors. This incorporation of observational errors enables us to compare the model to the observables much more physically and can now include more observable information like the error range of the kinematics. When the model is projected to the inclination of the target and compared with the observations of the system, accounting for the observational errors is vital to ensure χ^2 is measured correctly. This was achieved by changing the equation that calculates the deviation between the model and the target observables. From ST96, the FOC equation is given by

$$\Delta_j(t) \equiv \frac{y_i(t)}{Y_j} - 1, \tag{3.1.13}$$

DL07 replace this equation with

$$\Delta_j(t) \equiv \frac{y_i - Y_j}{\sigma(Y_j)}, \tag{3.1.14}$$

where $\sigma(Y_j)$ is the error in the target observable. With this definition of Δ_j, equation (3.1.7) now measures the absolute χ^2. If we now maximize equation (3.1.6) with respect to w_i, we find the following condition

$$\mu \frac{\partial S}{\partial w_i} - \sum_{j=1}^{J} \frac{K_{ji}}{\sigma(Y_j)} \Delta_j = 0. \tag{3.1.15}$$

From this we can now substitute into equation (3.1.10) to obtain the new equation for the FOC,

$$\frac{\mathrm{d}w_i(t)}{\mathrm{d}t} = \varepsilon w_i(t) \left[\mu \frac{\partial S}{\partial w_i} - \sum_{j=1}^{J} \frac{K_j[z_i(t)]}{\sigma(Y_j)} \Delta_j(t) \right]. \tag{3.1.16}$$

Thus, the weights will have converged when the terms in the brackets are balanced with respect to all w_i, i.e. when F is maximized. For large μ the weights will be smoothly distributed, however, this will likely compromise the convergence of χ^2.

Following DL07 we now characterize the solutions of equation (3.1.16) by using an argument similar to the one used in ST96. For small ε, the weights w_i will only change over many orbits, this means that we can orbit-average over the period $t_{orbit} \ll \tau \ll t_{orbit}/\varepsilon$. Thus, we can write the equation for the orbit-averaged $\bar{\Delta}_j$ as

$$\frac{\mathrm{d}\bar{\Delta}_j(t)}{\mathrm{d}t} = -\varepsilon \boldsymbol{A}_{jk} \bar{\Delta}_j(t), \tag{3.1.17}$$

with $\boldsymbol{A}$ being a matrix with elements given by

$$\boldsymbol{A}_{jk} = \Sigma_i \frac{\bar{K}_{ji}\bar{K}_{ki}}{\sigma_j \sigma_k} w_i(t). \tag{3.1.18}$$

However, near convergence there is little change in $w_i(t)$ with respect to time, therefore, we can replace it with a set of constants w_i^0 giving us

$$\boldsymbol{A}_{jk} = \Sigma_i \frac{\bar{K}_{ji}\bar{K}_{ki}}{\sigma_j \sigma_k} w_i^0. \tag{3.1.19}$$

The matrix $\boldsymbol{A}$ is symmetric as

$$\boldsymbol{A}_{jk} = \boldsymbol{A}_{kj} = \Sigma_i \frac{\bar{K}_{ki}\bar{K}_{ji}}{\sigma_k \sigma_j} w_i^0 = \Sigma_i \frac{\bar{K}_{ji}\bar{K}_{ki}}{\sigma_j \sigma_k} w_i^0, \tag{3.1.20}$$

therefore, as $\boldsymbol{A}$ is symmetric and real, it is Hermitian and thus the eigenvalues of $\boldsymbol{A}$ are also real. Equation (3.1.17) converges exponentially to $\bar{\Delta}_j(t) = 0$ at which point the weights have also converged. As in the previous section the modelling process will still suffer from temporal fluctuations, therefore, we need to incorporate a temporal smoothing function. ST96 imposed smoothing by effectively smearing the particle backwards along its orbit but inte-

grating the FOC over some smoothing time τ. However, in this case we do it more directly by simply integrating the observable y_j over the smoothing time, giving the smoothed FOC equation as

$$\tilde{\Delta}_j(t) \equiv \frac{\tilde{y}_i - Y_j}{\sigma(Y_j)}. \tag{3.1.21}$$

Where $\tilde{y}_i$ is the temporally smoothed observable obtained from

$$\tilde{y}_j(t) = \alpha \int_{\tau=0}^{\tau=\infty} y_j(t - \tau) e^{-\alpha\tau} \, d\tau. \tag{3.1.22}$$

This smooths the observables by effectively increasing the number of particles at each orbit. This means that our FOC should now change the particle weights much more consistently and not create large amounts of noise by adding and subtracting weight from the particle at a rate which is unreasonably fast.

Observables

For the target observables we use the following,

- coefficients of the spherical harmonic expansion,

- velocity and velocity dispersion obtained from the average of the best fitting Gaussian to the line of sight velocity distribution and its standard deviation, respectively,

- the higher order Gauss-Hermite moments h_3 and h_4.

These values will be discussed in more detail in the following sections.

Densities

For modelling the target distribution of stars we adopt a spherical harmonic expansion of the three-dimensional density (see appendix 1). The reason for this is that most NSCs are spheriodal, therefore, adopting a spherical harmonic scheme can greatly increase the
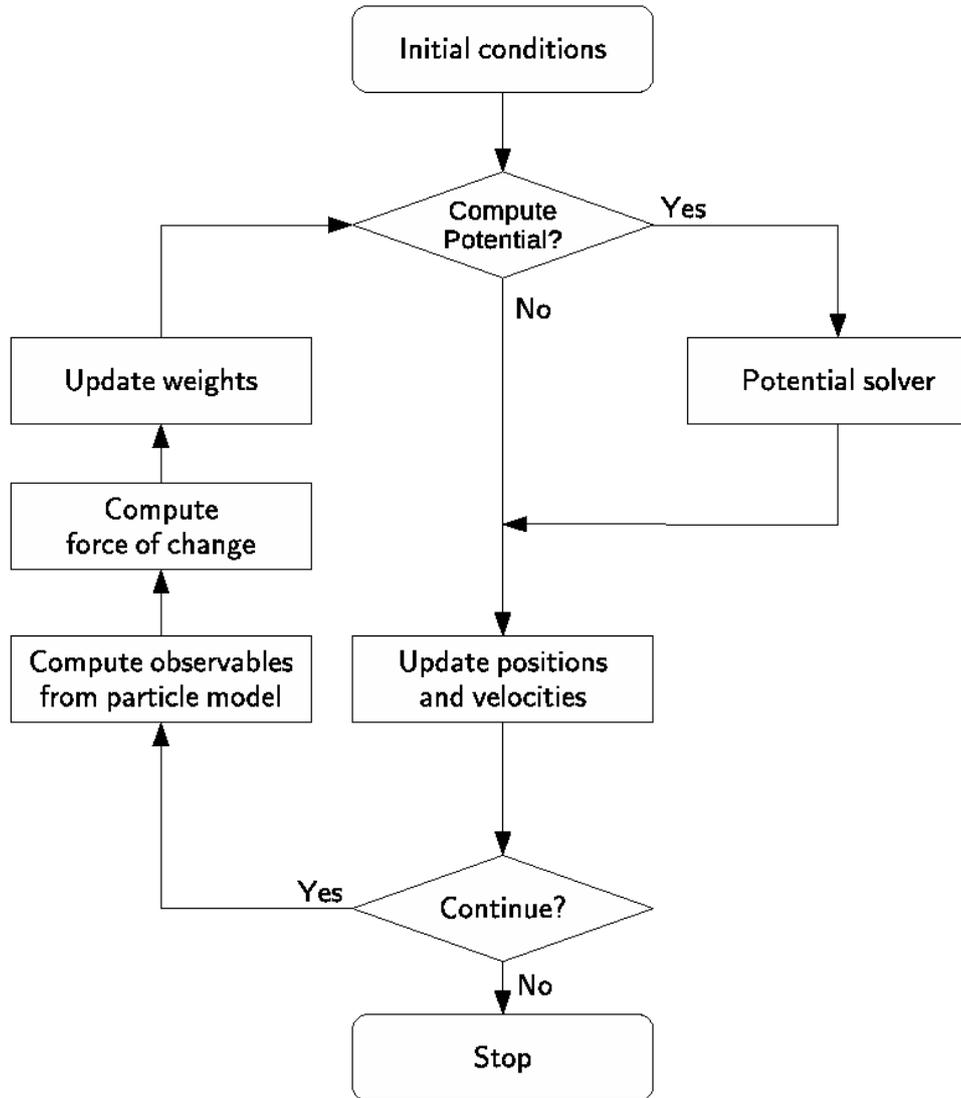
Fig. 3.1 A flow chart illustrating the internal workings of NMAGIC. The left side of the flow chart is the heart of the χ^2M2M algorithm, while the potential solver is generic for most modelling techniques and simply acts to move the particles along their orbits in the system's potential.

calculation speed of the differential equation solver. This is done by expanding the density in surface harmonics on a radial mesh of radii r_k. The expansion coefficients, A_{lm} are computed using a cloud-in-cell scheme. This means that the cell which may contain many particles is treated as a particle, where its kinematics and mass are given by the particles residing within

it. The contribution of the weight w_i of a particle at radius r, to the shell k, is defined as

$$
\gamma_k^{\text{CIC}}(r) = \begin{cases} \frac{r-r_{k-1}}{r_k-r_{k-1}}, & \text{if } r_{k-1} < r < r_k, \\[2mm] \frac{r_{k+1}-r}{r_{k+1}-r_k}, & \text{if } r_k < r < r_{k+1}, \\[2mm] 0, & \text{else.} \end{cases}
$$

Thus, the observable is the mass of each shell k given by

$$
m_k = M \sum_{i=1}^{N} w_i \gamma_k^{\text{CIC}}(r_i) \equiv M \sum_{i=1}^{N} w_i \gamma_{ki}^{\text{CIC}}. \tag{3.1.23}
$$

From this we can recognize the kernel for this set of observables is simply $K_{ij} = M\gamma_{ki}^{\text{CIC}}$. Therefore, the FOC can be thought of as the linear interpolation of the contributions of the two adjacent shells k_{i-1} and k_{i+1}. Thus, the FOC is given by the equation

$$
\Delta_k(m) = \frac{m_k - M_k}{\sigma(M_k)}, \tag{3.1.24}
$$

where M_k is the mass of shell k and $\sigma(M_k)$ is its error. The spherical harmonic coefficients, a_{lm}, for each cell of the particle model with $l > 0$ are given by

$$
a_{lm,k} = M \sum_{i=1}^{N} \gamma_{ki}^{\text{CIC}} Y_l^m(\theta_i, \phi_i) w_i. \tag{3.1.25}
$$

Thus, the kernel can be rewritten with respect to spherical harmonics giving

$$
K_{lm,ki} = M\gamma_{ki}^{\text{CIC}} Y_l^m(\theta_i, \phi_i). \tag{3.1.26}
$$

The FOC can also be rewritten with respect to spherical harmonics as

$$
\Delta_{lm,k}(a_{lm}) = \frac{a_{lm,k} - A_{lm,k}}{\sigma(A_{lm,k})}, \tag{3.1.27}
$$

with $A_{lm,k}$ as the target moments and $\sigma(A_{lm,k})$ the uncertainty.

Kinematics

The shape of the line-of-sight velocity profile can be approximated by a Gaussian (Gerhard 1993)[41] and therefore, an appropriate way to represent the velocity profile would be the use of a Gauss-Hermite expansion with coefficients h_n for $n = 1, \ldots, n_{max}$. To compare the model's kinematics to that of the target, we project the system to the inclination and position angle of the target system. As the bracketed terms in equation (3.1.10) must balance for the model to converge and have the correct units, the observables must have a mass component. Because of this constraint DL07 choose to use the mass-weighted Gauss-Hermite coefficients for the kinematic observables. From DL07 particle weights are assigned to a set of spatially distributed cells, $\mathscr{C}_p$. However, only certain particles will contribute to the kinematics and weight of a given cell, thus we define a selection function δ such that

$$\delta_{pi} = \begin{cases} 1, & \text{for } (y_i, z_i) \in \mathscr{C}_p, \\ 0, & \text{else.} \end{cases}$$

For the mass-weighted kinematic moments for each cell we have

$$b_{n,p} = m_p h_{n,p} \tag{3.1.28}$$

where m_p is the mass of cell $\mathscr{C}_p$ and $h_{n,p}$ is the respective Gauss-Hermite coefficient for the given cell. As in DL07 we define the velocity of each particle within a cell with respect to the mean light-of-sight velocity V_p and mean line-of-sight velocity dispersion σ_p of the cell from the best fitting Gaussian of the observational data such that

$$v_{pi} = \frac{v_{x,i} - V_p}{\sigma_p}, \tag{3.1.29}$$

and the mass of each cell is given by the sum

$$m_p = M \sum_{i=1}^{N} \delta_{pi} w_i. \tag{3.1.30}$$

From Gerhard (1993)[41] we adopt the set of dimensionless unnormalised Gauss-Hermite functions

$$u_n(v) = 1/(2^{n+1} \pi n)^{-1/2} H_n(v) \exp\frac{-v^2}{2}, \tag{3.1.31}$$

where H_n is the standard set of Hermite polynomials of the form

$$H_n(x) = (-1)^n e^{x^2} \frac{\mathrm{d}^n}{\mathrm{d}x^n} e^{-x^2}. \tag{3.1.32}$$

Therefore, the Gauss-Hermite coefficients are given by the sum

$$h_{n,p} = 2\sqrt{\pi} \sum_{i=1}^{N} \delta_{pi} u_n(v_{pi}). \tag{3.1.33}$$

Thus from equations (3.1.26), (3.1.28) & (3.1.31) we have that

$$b_{n,p} = 2\sqrt{\pi} \sum_{i=1}^{N} \delta_{pi}^2 u_n(v_{pi}) w_i, \tag{3.1.34}$$

however, δ_{pi} is unity or zero for all p & i, therefore,

$$b_{n,p} = 2\sqrt{\pi} \sum_{i=1}^{N} \delta_{pi} u_n(v_{pi}) w_i. \tag{3.1.35}$$

Again as for the densities we must introduce a kernel to ensure that when comparing the kinematics of the model to that of the observational data we are excluding the contribution of particles that should not contribute. Thus, for the mass-weighted higher-order Gauss-

Hermite moments, we construct the kernel

$$K_{n,pi} = 2\sqrt{\pi}M\delta_{pi}u_n(\upsilon_{pi}), \tag{3.1.36}$$

and the FOC is given by

$$\Delta_{n,p}[mh_n] = \frac{b_{n,p} - B_{n,p}}{\sigma(B_{n,p})}. \tag{3.1.37}$$

For an alternative to this approximation we follow the notation of van der Marel & Franx (1993)[101]. Here $\mathscr{L}$ is the unnormalised line of sight velocity distribution, with $\mathscr{L} = \gamma_0\mathscr{L}_0$ where $\mathscr{L}_0$ is the normalised line of sight velocity distribution and γ_0 is the total luminosity in the corresponding observational bin. From van der Marel & Franx (1993)[101], a well-behaved $\mathscr{L}$ can be expanded as

$$\mathscr{L}(\upsilon) = \gamma\frac{\alpha(w)}{\sigma}\sum_{i=0}^{N}h_iH_i(w), \tag{3.1.38}$$

with $\alpha(y)$ being a standard Gaussian, $w = (\upsilon - V)/\sigma$, and H_i are the Hermite polynomials. The h_i Gauss-Hermite moments depend on the particular choice of γ, V, σ and are given by

$$h_i = (2\sqrt{\pi})\frac{\gamma_0}{\gamma}\int_{-\infty}^{\infty}\mathscr{L}_o(\upsilon)\alpha(w)H_i(w)\,\mathrm{d}\upsilon. \tag{3.1.39}$$

This expansion converges as N tends towards infinity to the correct $\mathscr{L}$ for any γ, V and σ. However, it is often useful to get a good approximation for a finite N. Thus, we must choose γ, V and σ in a reasonable way. Typically, γ, V and σ are obtained from a best fitting Gaussian. For this choice of γ, V, and σ

$$h_0 = 1, \quad h_1 = h_2 = 0. \tag{3.1.40}$$

By imposing equation (3.1.40), van der Marel & Franx (1993)[101] replaced equation (3.1.38)

with

$$\mathcal{L}(\upsilon) = \gamma \frac{\alpha(w)}{\sigma} \left[1 + \sum_{i=3}^{N} h_i H_i(w) \right] \qquad (3.1.41)$$

We take V and σ to be the average and standard deviation, respectively, of the best fitting Gaussian to the line of sight velocity distribution. In a similar fashion to the van der Marel & Franx (1993)[101], we set $h_0 = 0$, $h_1 = h_2 = 0$. The target observables are obtained using the program pPXF from Cappellari & Emsellem (2004)[14] using the van der Marel & Franx (1993)[101] method. Because of this we also use this method for calculating the observables of the model.

Initial conditions

For the initial conditions of the model we choose a sphere with the major-axis density profile given by the target NSC. The mass density is normalized by setting the mass-to-light ratio to unity and the gravitational potential is computed. Following Gerhard (1991)[40], the isotropic DF is computed and integrated to generate a set of 0.75M equal mass particles. A benefit of M2M is that, because of the particle splitting, the initial conditions of the model do not need to be very close to the final model. This means that as a particles' weight increases it becomes increasingly likely that the particle will be subdivided into n particles of weight $w_n = w/n$, subject to $w/n \approx w_0$. Moreover, as the weight of a particle decreases it becomes increasingly likely that the particle will be removed from the model. This method of particle splitting, or resampling, is explained in more detail in Dehnen (2009)[28].

Chapter 4

Results

4.1 Single component model of NGC 4244

To ensure that NMAGIC was producing reasonable models, we constructed a number of single component models of NGC 4244 using similar data to that used to model NGC 4244 in DL13. We constructed models with various mass-to-light ratios (M/L_{NSC}) for the NSC, and with different BH masses (see Table 3.1).

4.1.1 Deprojection

To adequately model the luminosity distribution of a stellar system, we must know to a reasonable level the three-dimensional density distribution. However, direct observations only give a two-dimensional distribution. Thus, we need to convert the two-dimensional projected luminosity distribution into a three-dimensional distribution for each component individually to model them. The projected surface brightness can be thought of as the integral of the deprojected surface brightness with respect to z, therefore, we can say

$$I(R) = \int_{-\infty}^{\infty} \rho(r) \, \mathrm{d}z, \qquad (4.1.1)$$

where $I(R)$ is the projected surface brightness at projected radius R and $\rho(r)$ is the brightness at spatial radius r. With $r^2 = z^2 + R^2$, using the chain rule

$$dz = \frac{d}{dr}\sqrt{r^2 - R^2}\,dr = \frac{r\,dr}{\sqrt{r^2 - R^2}}. \tag{4.1.2}$$

Substituting equation (4.1.2) into equation (4.1.1) gives

$$I(R) = \int_R^\infty \Sigma(r)\frac{r\,dr}{\sqrt{r^2 - R^2}}. \tag{4.1.3}$$

This is an Abel integral and as such we can invert the equation to give it in terms of $\Sigma(r)$ as

$$\Sigma(R) = -\frac{1}{\pi}\int_r^\infty \frac{dI}{dR}(R)\frac{dR}{(\sqrt{r^2 - R^2})}, \tag{4.1.4}$$

Equation (4.1.4) assumes spherical symmetry which, for many systems, is not a valid assumption.

The deprojection of an exponential disc profile is given by van der Kruit & Searle (1981)[99], to be

$$\rho(R,z) = \rho_0 e^{-R/h_r}\text{sech}^2(z/z_0), \tag{4.1.5}$$

where $\rho_0 = \Sigma_0/(2h_r)$, h_e is the effective radius, and z_0 a scale parameter. This can be applied to the main disc of the galaxy (MD) and NCD of the NSC, however, the deprojection of a Sérsic, ring or King profile for the NCS are more complex to deproject analytically (these different surface brightness profiles are discussed in section 2.2). Therefore, we use the program of Magorrian (1999)[65] to numerically deproject the surface brightness profile of the NCS. The program fits a smooth axisymmetric density distribution to the surface brightness distribution at a given inclination. However, as the deprojection is being calculated numerically, the reprojected surface brightness profile might not match the fitted surface brightness profile perfectly.

Comp.	Σ_0 $[L_\odot \mathrm{pc}^{-2}]$	ρ_0 $[L_\odot \mathrm{pc}^{-3}]$	h_r [pc]	z_0 [pc]	q	I_e $[L_\odot \ \mathrm{pc}^{-2}]$	r_e [pc]	n
MD	598	0.167	1783	469				
NCD	1.41×10^5	2.08×10^4	3.39	1.19				
NCS					0.81	8.73×10^3	10.86	1.68

Table 4.1 Parameters for the best fitting three-component model NGC 4244 from [24,89,91]. The main disc (MD) and nuclear cluster disc (NCD) are fitted by two exponential disc profiles, while the nuclear cluster spheroidal (NCS) is fitted by a Sérsic profile. However, due to the volume density of the NSC being around a million times greater than that of the MD[89] we neglect the effect of the MD when fitting the observational data.

4.1.2 Density

We used the deprojection code of Magorrian (1999)[65] to produce a deprojected surface brightness profile from isophotes fit by a two component Sérsic and disc profile (see table 3.1 for the fit parameters), assuming an inclination of $90°$ from Table 2.1. The deprojected SB is plotted in Figure (4.2).
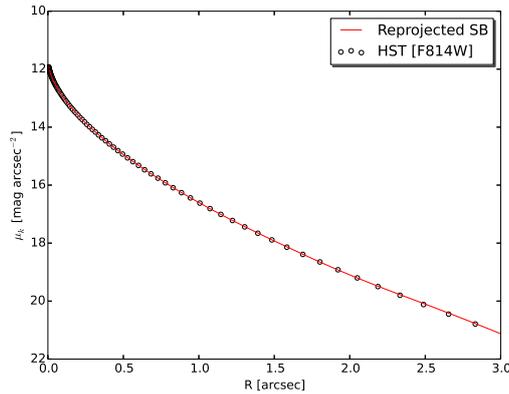
Fig. 4.1 Comparison of the deprojected SB profile of the NSC compared to the observational fit from *HST* data in the F814W band.

To check the deprojection we compare the reprojected SB profile with the fitted obser-vational data in Figure (4.3). The deprojected luminosity profile is in good agreement with

its projected counterpart. For the this thesis we treat the three-component profile as a single component. We assume that the mass distribution follows the luminosity distribution for a given mass-to-light ratio $M/L_{NSC} = 1.3$ given by DL13 as the best fitting mass-to-light ratio for the NCS. We now employ a three-dimensional spherical harmonic expansion scheme described in section (3.1.1). With this density distribution in our spherical harmonic scheme we can now model it using NMAGIC. To produce this initial population we use the method from Lucy (1974)[61] (see box 3.1.1) to compute the distribution function from the spherical density distribution.
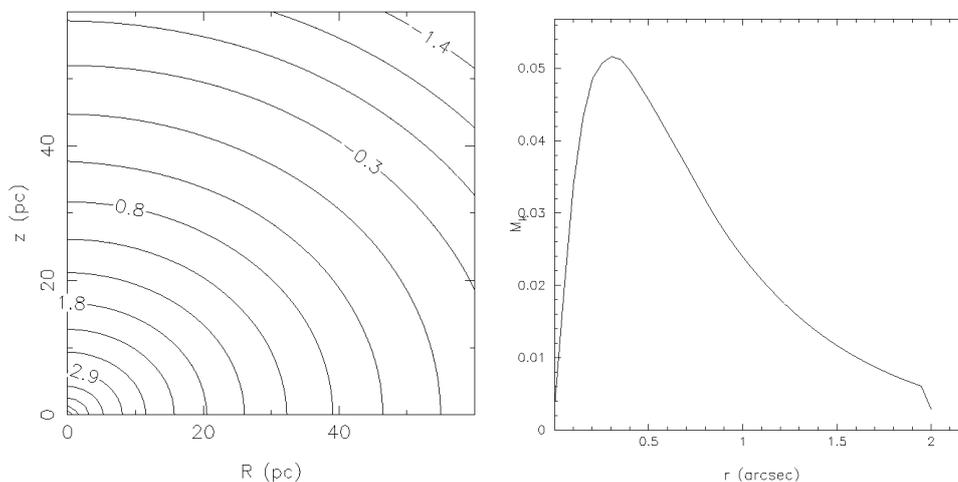
Fig. 4.2 Left: Deprojected luminosity contour plot of our single component fit for NGC 4244. Right: the deprojected mass distribution of NGC 4244 used as observables for modelling with NMAGIC.

4.1.3 Kinematics

To improve our model we also include the kinematics of NGC 4244 as extra observables for the model to be constrained by. For the kinematics we use the line-of-sight velocity, velocity dispersion, and the higher order Gauss-Hermite coefficients h_3 and h_4, given by the Gemini NIFS data and reduced using IRAF and IDL by Anil Seth (see chapter 2) for DL13.

However, we also need to include the possibility of the NSC hosting a black hole. This

is done by modelling the central black hole using a Plummer model. We choose a Plummer sphere as it is well suited to describe a spherical system that has constant density at small radii, and the density falls off to zero at large radii. The potential of a Plummer model is given by

$$\phi = -\frac{GM}{\sqrt{r^2 + b^2}}, \tag{4.1.6}$$

where G is the gravitational constant, M is the total mass of the system (or in this case the mass of the black hole), r is the radius, and b is the Plummer scale length (Binney & Tremaine 2008)[7].The addition of a black hole will greatly change the dynamics of the system, therefore, we must take care when we first add it to the potential of the system. As such we adiabatically implement the potential of the black hole over some growth time. We set $b = 0.1$ pc for NGC 4244 and ran 29 models of NGC 4244 using different mass-to-light ratios and different black hole masses with NAMGIC (see table 3.2 & figure 3.5).

The number of particles for each run is set to be $N_p = 7.5 \times 10^6$ and the integration scheme was based on the Runge-Kutta method for approximating ordinary differential equations. We set the dimensionless constants required by the made-to-measure method to be, $\varepsilon = 0.02$, $\mu = 0.2 \times 10^{-6}$, $\alpha = 2.1\varepsilon$ and the set of priors are given by $w_0 = 1$.

The density distribution of our models fit the deprojected distribution obtained from *HST* data in the F814W band. To compare our single component models to the observational data we plot the luminosity-weighted kinematic data from run 007 (see table 4.2) and compare to the symmetrized NIFS integral-field kinematic data of NGC 4244 in figure 4.5. For comparison we also include the similar plot from DL13 in which they compare two of their multi-component models to the symmetrized NIFS integral-field kinematic data of NGC 4244, one of which contained a black hole of mass $3.0 \times 10^5 \, \mathrm{M_\odot}$. We find that our single component models compare well to the multi-component models of DL13.

We also find that our models can converge to the observational data for NGC 4244 while including the potential of a central black hole of mass $\sim 5 \times 10^5 \, \mathrm{M_\odot}$. However, when we

Model	BH Mass [$M_\odot$]	M/L_{NSC}	χ^2	$\chi^2_{reduced}$
006	3.2×10^4	1.7	227	0.622
007	6.5×10^4	1.7	235	0.643
008	1.3×10^5	1.7	351	0.688
009	3.2×10^4	1.5	223	0.611
010	6.5×10^4	1.5	219	0.601
011	1.3×10^5	1.5	219	0.601
012	3.2×10^4	1.3	308	0.843
013	6.5×10^4	1.3	290	0.794
014	1.3×10^5	1.3	263	0.722
015	3.2×10^4	1.9	281	0.77
016	6.5×10^4	1.9	296	0.811
017	1.3×10^5	1.9	326	0.894
018	0	1.3	332	0.910
019	0	1.5	236	0.646
020	0	1.7	225	0.620
021	0	1.9	269	0.737
022	2.5×10^5	1.3	237	0.648
023	2.5×10^5	1.5	231	0.634
024	2.5×10^5	1.7	290	0.795
025	2.5×10^5	1.9	383	1.048
027	5.0×10^5	1.3	234	0.64
028	5.0×10^5	1.5	279	0.765
029	5.0×10^5	1.7	372	1.019
030	5.0×10^5	1.9	485	1.33
031	1.0×10^6	1.3	683	1.87
032	1.0×10^6	1.5	402	1.10
033	1.0×10^6	1.7	402	1.10
034	1.0×10^6	1.9	413	1.13
035	2.0×10^6	1.3	508	1.39
035	2.0×10^6	1.5	664	1.82
035	2.0×10^6	1.7	814	2.23
035	2.0×10^6	1.9	923	2.53

Table 4.2 Converged NMAGIC models of NGC 4244 including density and kinematics. The set of models contain central black holes spans mass range $3 \times 10^4 - 2 \times 10^6$, from IMBHs to low mass SMBH. Covering the mass-to-light ratio values of 1.3–1.9. The values for $\chi^2_{reduced}$ are based on 365 observables for the kinematics.
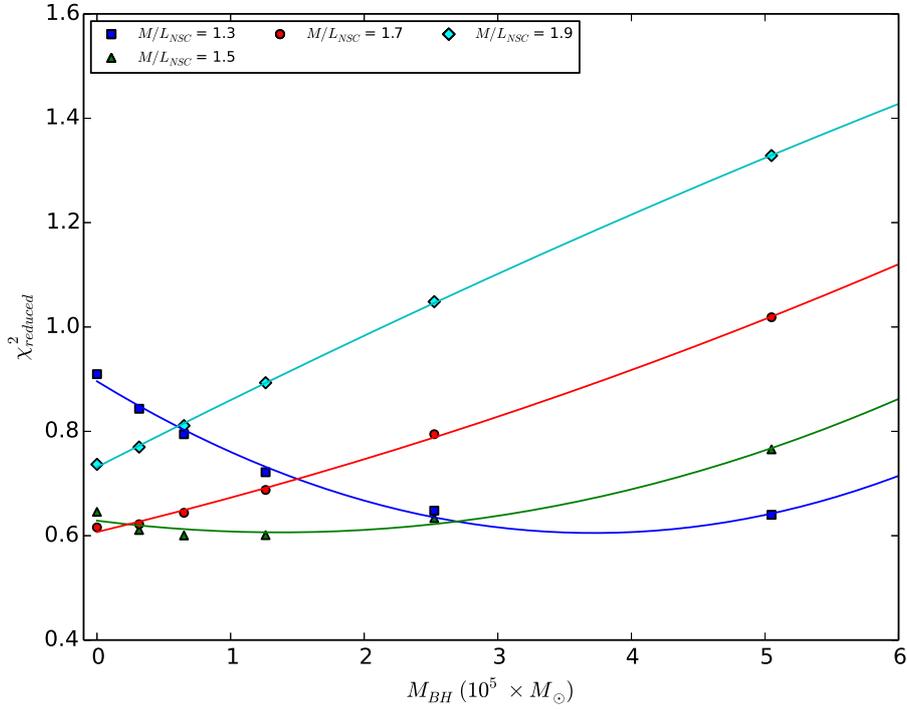
Fig. 4.3 Reduced χ^2 versus nuclear black hole mass for different mass-to-light ratios for the NSC of NGC 4244. For high mass-to-light ratios the χ^2 grows as the black hole mass increases, however, for a lower mass-to-light ratio as the black hole mass increases we find χ^2 decreasing.

go to higher mass-to-light ratios $M/L_{NSC} > 1.3$ it becomes harder to match the observables when including a central black hole. A similar result was found by the multi-component models of DL13. Moreover, when we look at the internal kinematics of the NSC we find that we reproduce the negative vertical anisotropy found in the multi-component model of DL13 (see figure 4.4).
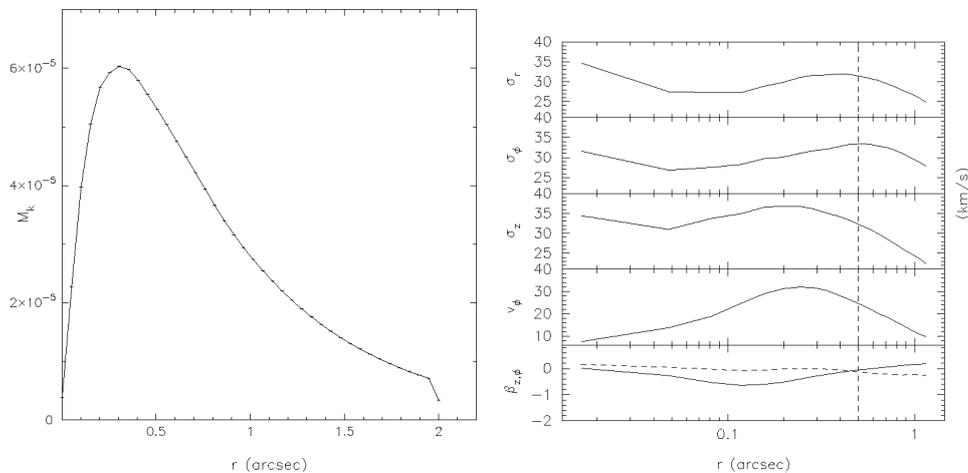
Fig. 4.4 Two plots of run 007, which has a BH mass of $6.5 \times 10^4 \, \mathrm{M_\odot}$, a mass-to-light ratio of $M/L_{NSC} = 1.7$ and a reduced χ^2 of 0.643 (based on 365 observables for the kinematics). Left: the line is the mass distribution of the model and the dashes represent the target distribution from the deprojection of the surface brightness from the *HST* in the F814W band. Right: from top to bottom, velocity dispersion σ with respect to each cylindrical coordinate r, ϕ and z, the rotational velocity v_ϕ and the vertical anisotropy β_z.
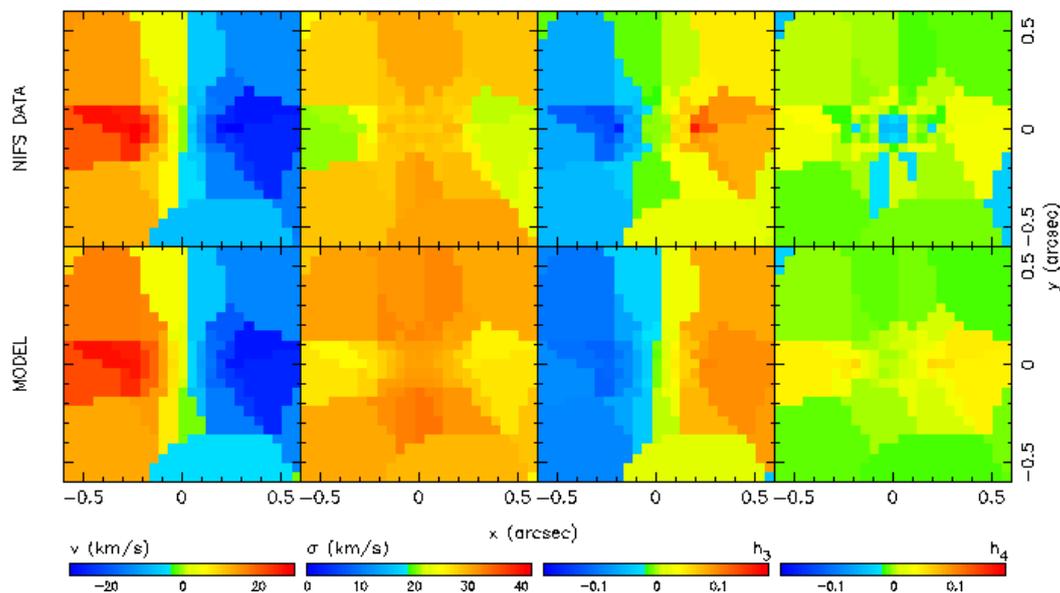
Fig. 4.5 Top: the symmetrized NIFS integral-field kinematic data of NGC 4244 within ± 0.7 arcsec of the centre, bottom: luminosity-weighted kinematic data taken from run 007, which has a BH mass of $6.5 \times 10^4 \, \mathrm{M_\odot}$, a mass-to-light ratio of $M/L_{NSC} = 1.7$. From right to left the maps show, line-of-sight velocity v, line-of-sight velocity dispersion σ and higher the order Gauss-Hermite moments h_3 and h_4.

48
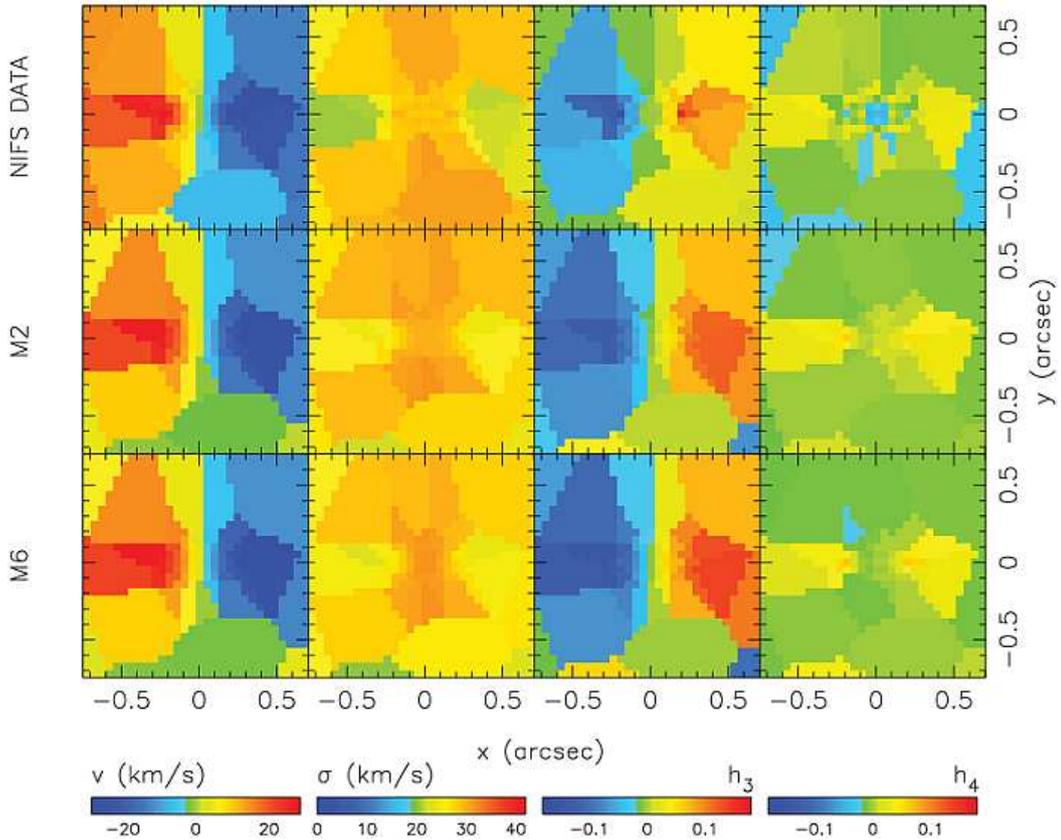
Fig. 4.6 Figure taken from De Lorenzi et al. (2013)[24] for comparison. Top: the symmetrized NIFS integral-field kinematic data of NGC 4244 within ± 0.7 arcsec of the centre. Middle: luminosity-weighted kinematic data taken from the best fitting model M2 with the mass-to-light ratio of $M/L_{NSC} = 1.3$ and no central BH. Bottom: luminosity-weighted kinematic data taken from the best fitting model M6 with the mass-to-light ratio of $M/L_{NSC} = 1.3$ and a central BH of mass $M_{BH} = 3.0 \times 10^5 \, \mathrm{M}_\odot$. From right to left the maps show, line-of-sight velocity υ, line-of-sight velocity dispersion σ and higher the order Gauss-Hermite moments h_3 and h_4.

4.2   Preliminary results for M33

As described in chapter 3, to accurately model the distribution of stars in an inclined galaxy or NSC we must first deproject the density distribution to obtain the intrinsic three-dimensional distribution. We take the luminosity distribution from the F814W band of *HST* and now deproject the luminosity using the code of Magorrian (1999)[65]. Again here the reprojected luminosity distribution is not an exact match to the observed data illustrated in figure (4.3). In a similar way to chapter 3 we assume a mass-to-light ratio for the nuclear star cluster M/L_{NSC}, which enables us to transit from surface brightness to density. Figure 4.7 shows the comparison between the reprojected luminosity distribution and the observed projected luminosity distribution and figure 4.8 shows the deprojected luminosity contours and the corresponding mass distribution.
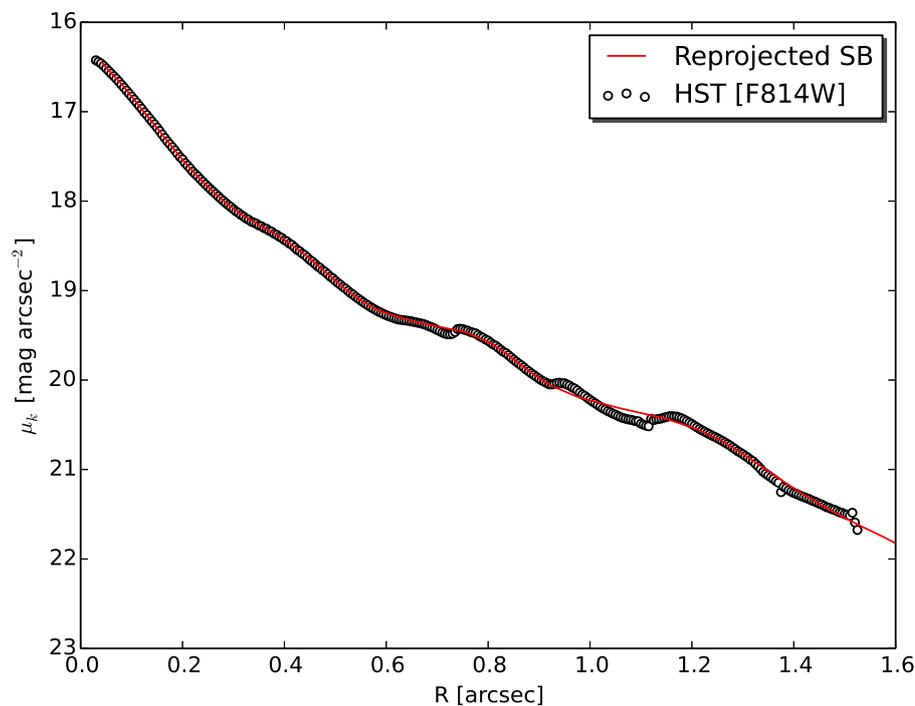
Fig. 4.7 Reprojected surface brightness of M33 compared with the observed surface brightness from *HST* data in the F814W band.

Fig. 4.8 Left: Deprojected luminosity contour plot of our single component fit for M33 based on data from the *HST* in the F814W band. Right: the deprojected mass distribution of M33 used as observables for modelling with NMAGIC.

With this deprojected density distribution we now expand the density in spherical harmonics as described in chapter 3. For our model we also require an initial population of particles for the model to be reweighted in order to match the density distribution. To produce this initial population we use the method from Lucy (1974)[61] (see box 3.1.1) to compute the distribution function from the spherical density distribution. With this distribution function we must now define some set of particles with equal mass, spaced with respect to the distribution function (i.e. in higher density regions the particles will be more closely spaced then in a less dense region). We then constructed a density model from these data using NMAGIC. In a similar fashion to the model for NGC 4244 the number of particles for each run is set to be $N_p = 7.5 \times 10^6$ and the integration scheme was based on the Runge-Kutta method. We also set the constants required by the made-to-measure method to be, $\varepsilon = 0.02$, $\mu = 0.2 \times 10^{-6}$, $\alpha = 2.1\varepsilon$ and the set of priors are given by $w_0 = 1$. Figure 4.9 shows the evolution of χ^2 as the model converges to the target's deprojected density distribution and the models mass distribution once it has converged.
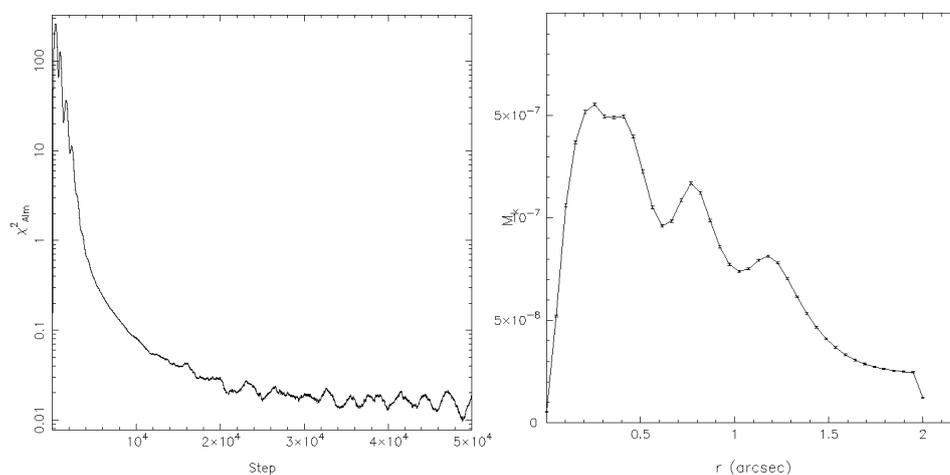
Fig. 4.9 Left: evolution of reduced $\chi^2_{A_{lm}}$ during the modelling run. Right: mass distribution of our density model is shown by the line and the dashes represent the target distribution from the deprojection of the surface brightness from the *HST* in the F814W band.

Chapter 5

Conclusions and discussion

5.1   Single component models of NGC 4244

Our single component models of NGC 4244 based on the NIFS integral-field kinematics and *HST* F814W band data, agree with the two component disc and Sérsic models of DL13. We can conclude from this that the inclusion of the separate disc component does not have a large effect on the constrained quantities produced by NMAGIC. However, this may be because of the low mass of the disc compared to the spheroid. DL13 found that for NGC 4244 the mass of the NSC was at least ten times that of the NCD. For NSCs that contain more dominant NCDs the multi-component model may fit far better than a single component model.

   We have shown that the NSC could host a black hole with a mass upper limit of $5 \times 10^5\,\mathrm{M}_\odot$ as long as the mass-to-light ratio is ≤ 1.5, this agrees with the finding of DL13. Moreover, the best fitting mass-to-light ratio for the NSC is $M/L_{NSC} \simeq 1.3$, therefore, we can conclude that is possible that the NSC hosts a central black hole with an upper limit of $5 \times 10^5\,\mathrm{M}_\odot$, which is only one order of magnitude away from being considered a SMBH. As NGC 4244 is a bulgeless galaxy, hosting a black hole this massive would put it in a very select group, but is also consistent with observations.

We also find a negative vertical anisotropy ($\beta_z < 0$) in the inner 1 arc second. This result is similar to that found by DL13 for the multi-component model. Therefore, it might be reasonable to assume that the multi-component nature of the NSC is not responsible for this negative vertical anisotropy. DL13 also checked that this negative vertical anisotropy was not a projection effect by modelling the NSC at different inclinations and still found ($\beta_z < 0$). This check would also be useful for our single component model.

5.1.1 Future work

Including kinematics in the model of M33

So far we have created models for M33 that only converge to the density distribution given by the *HST* F814W band data. The natural progression would be to include the NIFS integral-field kinematic data, in a similar way to the modelling of NGC 4244, as additional observables to constrain the model. Figure 6.1 shows the symmetrized kinematic data for M33.
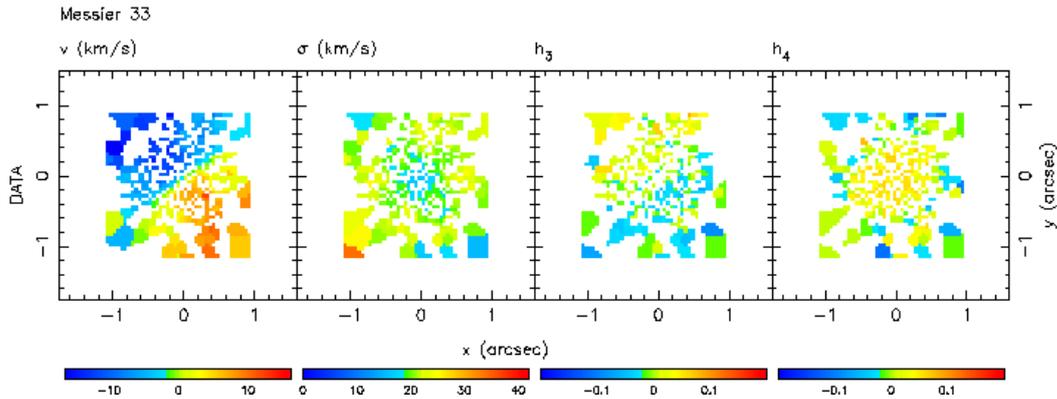
Fig. 5.1 Symmetrized NIFS integral-field kinematic data of M33 within ± 1 arcsec of the centre. From right to left the maps show, line-of-sight velocity υ, line-of-sight velocity dispersion σ and higher the order Gauss-Hermite moments h_3 and h_4.

After including the kinematic data we could measure the internal kinematics and the vertical anisotropy. This would allow us to determine if the vertical anisotropy of NGC

4244 is an effect of our modelling technique or if the NSC of NGC 4244 is in a special state of its evolution. The addition of a black hole to our density models of M33 yields very little information, however, adding a central black hole to models contained by both density and kinematics could lead us to an upper limit on the black hole mass at the centre of M33.

References

(1) Andersen, D. R., Walcher, C. J., Böker, T., Ho, L. C., van der Marel, R. P., Rix, H.-W., and Shields, J. C. (2008). Caught in Formation: The Nuclear-Cluster-to-Be in NGC 2139. *ApJ*, 688:990–999.

(2) Balick, B. and Brown, R. L. (1974). Intense sub-arcsecond structure in the galactic center. *ApJ*, 194:265–270.

(3) Barth, A. J., Strigari, L. E., Bentz, M. C., Greene, J. E., and Ho, L. C. (2009). Dynamical Constraints on the Masses of the Nuclear Star Cluster and Black Hole in the Late-Type Spiral Galaxy NGC 3621. *ApJ*, 690:1031–1044.

(4) Binggeli, B., Sandage, A., and Tammann, G. A. (1985). Studies of the Virgo Cluster. II - A catalog of 2096 galaxies in the Virgo Cluster area. *AJ*, 90:1681–1759.

(5) Binney, J. and Mamon, G. A. (1982). M/L and velocity anisotropy from observations of spherical galaxies, or must M87 have a massive black hole. *MNRAS*, 200:361–375.

(6) Binney, J. and Tremaine, S. (1987). *Galactic dynamics*. Princeton University Press.

(7) Binney, J. and Tremaine, S. (2008). *Galactic Dynamics: Second Edition*. Princeton University Press.

(8) Binney, J. J., Davies, R. L., and Illingworth, G. D. (1990). Velocity mapping and models of the elliptical galaxies NGC 720, NGC 1052, and NGC 4697. *ApJ*, 361:78–97.

(9) Bissantz, N., Debattista, V. P., and Gerhard, O. (2004). Large-Scale Model of the Milky Way: Stellar Kinematics and the Microlensing Event Timescale Distribution in the Galactic Bulge. *ApJ*, 601:L155–L158.

(10) Böker, T. (2010). Nuclear star clusters. In de Grijs, R. and Lépine, J. R. D., editors, *IAU Symposium*, volume 266 of *IAU Symposium*, pages 58–63.

(11) Böker, T., Laine, S., van der Marel, R. P., Sarzi, M., Rix, H.-W., Ho, L. C., and Shields, J. C. (2002). A Hubble Space Telescope Census of Nuclear Star Clusters in Late-Type Spiral Galaxies. I. Observations and Image Analysis. *AJ*, 123:1389–1410.

(12) Böker, T., Sarzi, M., McLaughlin, D. E., van der Marel, R. P., Rix, H.-W., Ho, L. C., and Shields, J. C. (2004). A Hubble Space Telescope Census of Nuclear Star Clusters in Late-Type Spiral Galaxies. II. Cluster Sizes and Structural Parameter Correlations. *AJ*, 127:105–118.

(13) Cappellari, M. (2008). Measuring the inclination and mass-to-light ratio of axisymmetric galaxies via anisotropic Jeans models of stellar kinematics. *MNRAS*, 390:71–86.

(14) Cappellari, M. and Emsellem, E. (2004). Parametric Recovery of Line-of-Sight Velocity Distributions from Absorption-Line Spectra of Galaxies via Penalized Likelihood. *PASP*, 116:138–147.

(15) Capuzzo-Dolcetta, R. and Miocchi, P. (2008). Self-consistent simulations of nuclear cluster formation through globular cluster orbital decay and merging. *MNRAS*, 388:L69–L73.

(16) Carollo, C. M., Stiavelli, M., de Zeeuw, P. T., and Mack, J. (1997). Spiral Galaxies with WFPC2.I.Nuclear Morphology, Bulges, Star Clusters, and Surface Brightness Profiles. *AJ*, 114:2366.

(17) Chandrasekhar, S. (1943). Dynamical Friction. I. General Considerations: the Coefficient of Dynamical Friction. *ApJ*, 97:255.

(18) Ciotti, L. and Bertin, G. (1999). Analytical properties of the $R^{1/m}$ law. *A&A*, 352:447–451.

(19) Corbelli, E., Lorenzoni, S., Walterbos, R., Braun, R., and Thilker, D. (2010). A wide-field H I mosaic of Messier 31. II. The disk warp, rotation, and the dark matter halo. *A&A*, 511:A89.

(20) Côté, P., Piatek, S., Ferrarese, L., Jordán, A., Merritt, D., Peng, E. W., Haşegan, M., Blakeslee, J. P., Mei, S., West, M. J., Milosavljević, M., and Tonry, J. L. (2006). The ACS Virgo Cluster Survey. VIII. The Nuclei of Early-Type Galaxies. *ApJS*, 165:57–94.

(21) de Lorenzi, F., Debattista, V. P., Gerhard, O., and Sambhus, N. (2007). NMAGIC: a fast parallel implementation of a χ^2-made-to-measure algorithm for modelling observational data. *MNRAS*, 376:71–88.

(22) de Lorenzi, F., Gerhard, O., Coccato, L., Arnaboldi, M., Capaccioli, M., Douglas, N. G., Freeman, K. C., Kuijken, K., Merrifield, M. R., Napolitano, N. R., Noordermeer, E., Romanowsky, A. J., and Debattista, V. P. (2009). Dearth of dark matter or massive dark halo? Mass-shape-anisotropy degeneracies revealed by NMAGIC dynamical models of the elliptical galaxy NGC 3379. *MNRAS*, 395:76–96.

(23) de Lorenzi, F., Gerhard, O., Saglia, R. P., Sambhus, N., Debattista, V. P., Pannella, M., and Méndez, R. H. (2008). Dark matter content and internal dynamics of NGC 4697: NMAGIC particle models from slit data and planetary nebula velocities. *MNRAS*, 385:1729–1748.

(24) De Lorenzi, F., Hartmann, M., Debattista, V. P., Seth, A. C., and Gerhard, O. (2013). Three-integral multicomponent dynamical models and simulations of the nuclear star cluster in NGC 4244. *MNRAS*, 429:2974–2985.

(25) de Vaucouleurs, G. (1948). Recherches sur les Nebuleuses Extragalactiques. *Annales d'Astrophysique*, 11:247.

(26) de Vaucouleurs, G. (1959). Photoelectric Photometry of Messier 33 IN the u, b, v, System. *ApJ*, 130:728.

(27) de Vaucouleurs, G., de Vaucouleurs, A., Corwin, Jr., H. G., Buta, R. J., Paturel, G., and Fouqué, P. (1991). *Third Reference Catalogue of Bright Galaxies. Volume I: Explanations and references. Volume II: Data for galaxies between 0^h and 12^h. Volume III: Data for galaxies between 12^h and 24^h*. Springer; 1st Edition.

(28) Dehnen, W. (2009). Tailoring triaxial N-body models via a novel made-to-measure method. *MNRAS*, 395:1079–1086.

(29) Duncan, M. J. and Wheeler, J. C. (1980). Anisotropic velocity distributions in M87 - Is a supermassive black hole necessary. *ApJ*, 237:L27–L31.

(30) Emsellem, E. (2013). Is the black hole in NGC 1277 really overmassive? *MNRAS*, 433:1862–1870.

(31) Emsellem, E. and van de Ven, G. (2008). Formation of Central Massive Objects via Tidal Compression. *ApJ*, 674:653–659.

(32) Erwin, P. and Gadotti, D. A. (2012). Do Nuclear Star Clusters and Supermassive Black Holes Follow the Same Host-Galaxy Correlations? *Advances in Astronomy*, 2012.

(33) Farrell, S. A., Webb, N. A., Barret, D., Godet, O., and Rodrigues, J. M. (2009). An intermediate-mass black hole of over 500 solar masses in the galaxy ESO243-49. *Nature*, 460:73–75.

(34) Feldmeier, A., Neumayer, N., Seth, A., Schödel, R., Lützgendorf, N., de Zeeuw, P. T., Kissler-Patig, M., Nishiyama, S., and Walcher, C. J. (2014). Large scale kinematics and dynamical modelling of the Milky Way nuclear star cluster. *ArXiv e-prints*.

(35) Ferrarese, L., Côté, P., Dalla Bontà, E., Peng, E. W., Merritt, D., Jordán, A., Blakeslee, J. P., Haşegan, M., Mei, S., Piatek, S., Tonry, J. L., and West, M. J. (2006). A Fundamental Relation between Compact Stellar Nuclei, Supermassive Black Holes, and Their Host Galaxies. *ApJ*, 644:L21–L24.

(36) Ferrarese, L. and Merritt, D. (2000). A Fundamental Relation between Supermassive Black Holes and Their Host Galaxies. *ApJ*, 539:L9–L12.

(37) Gebhardt, K., Bender, R., Bower, G., Dressler, A., Faber, S. M., Filippenko, A. V., Green, R., Grillmair, C., Ho, L. C., Kormendy, J., Lauer, T. R., Magorrian, J., Pinkney, J., Richstone, D., and Tremaine, S. (2000). A Relationship between Nuclear Black Hole Mass and Galaxy Velocity Dispersion. *ApJ*, 539:L13–L16.

(38) Gebhardt, K., Lauer, T. R., Kormendy, J., Pinkney, J., Bower, G. A., Green, R., Gull, T., Hutchings, J. B., Kaiser, M. E., Nelson, C. H., Richstone, D., and Weistrop, D. (2001). M33: A Galaxy with No Supermassive Black Hole. *AJ*, 122:2469–2476.

(39) Geha, M., Guhathakurta, P., and van der Marel, R. P. (2002). Internal Dynamics, Structure, and Formation of Dwarf Elliptical Galaxies. I. A Keck/Hubble Space Telescope Study of Six Virgo Cluster Dwarf Galaxies. *AJ*, 124:3073–3087.

(40) Gerhard, O. E. (1991). A new family of distribution functions for spherical galaxies. *MNRAS*, 250:812–830.

(41) Gerhard, O. E. (1993). Line-of-sight velocity profiles in spherical galaxies: breaking the degeneracy between anisotropy and mass. *MNRAS*, 265:213.

(42) Ghez, A. M., Salim, S., Weinberg, N. N., Lu, J. R., Do, T., Dunn, J. K., Matthews, K., Morris, M. R., Yelda, S., Becklin, E. E., Kremenek, T., Milosavljevic, M., and Naiman, J. (2008). Measuring Distance and Properties of the Milky Way's Central Supermassive Black Hole with Stellar Orbits. *ApJ*, 689:1044–1062.

(43) Gillessen, S., Eisenhauer, F., Fritz, T. K., Bartko, H., Dodds-Eden, K., Pfuhl, O., Ott, T., and Genzel, R. (2009). The Orbit of the Star S2 Around SGR A* from Very Large Telescope and Keck Data. *ApJ*, 707:L114–L117.

(44) Graham, A. W. (2001). An Investigation into the Prominence of Spiral Galaxy Bulges. *AJ*, 121:820–840.

(45) Graham, A. W. and Scott, N. (2013). The M $_{BH}$-L $_{spheroid}$ Relation at High and Low Masses, the Quadratic Growth of Black Holes, and Intermediate-mass Black Hole Candidates. *ApJ*, 764:151.

(46) Grant, N. I., Kuipers, J. A., and Phillipps, S. (2005). Nucleated dwarf elliptical galaxies in the Virgo cluster. *MNRAS*, 363:1019–1030.

(47) Gültekin, K., Richstone, D. O., Gebhardt, K., Lauer, T. R., Tremaine, S., Aller, M. C., Bender, R., Dressler, A., Faber, S. M., Filippenko, A. V., Green, R., Ho, L. C., Kormendy, J., Magorrian, J., Pinkney, J., and Siopis, C. (2009). The M-σ and M-L Relations in Galactic Bulges, and Determinations of Their Intrinsic Scatter. *ApJ*, 698:198–221.

(48) Harris, W. E. (2009). The Globular Cluster System in M87: A Wide-Field Study with CFHT/Megacam. *ApJ*, 703:939–950.

(49) Harris, W. E., Allwright, J. W. B., Pritchet, C. J., and van den Bergh, S. (1991). The luminosity distribution of globular clusters in three giant Virgo ellipticals. *ApJS*, 76:115–151.

(50) Hartmann, M., Debattista, V. P., Seth, A., Cappellari, M., and Quinn, T. R. (2011). Constraining the role of star cluster mergers in nuclear cluster formation: simulations confront integral-field data. *MNRAS*, 418:2697–2714.

(51) Jarrett, T. H., Chester, T., Cutri, R., Schneider, S. E., and Huchra, J. P. (2003). The 2MASS Large Galaxy Atlas. *AJ*, 125:525–554.

(52) Jeans, J. H. (1915). On the theory of star-streaming and the structure of the universe. *MNRAS*, 76:70–84.

(53) Kamann, S., Wisotzki, L., Roth, M. M., Gerssen, J., Husser, T.-O., Sandin, C., and Weilbacher, P. (2014). The central dynamics of M3, M13, and M92: stringent limits on the masses of intermediate-mass black holes. *A&A*, 566:A58.

(54) King, I. R. (1978). Surface photometry of elliptical galaxies. *ApJ*, 222:1–13.

(55) Kissler-Patig, M. and Gebhardt, K. (1998). The Spin of M87 as Measured from the Rotation of its Globular Clusters. *AJ*, 116:2237–2245.

(56) Kormendy, J., Bender, R., and Cornell, M. E. (2011). Supermassive black holes do not correlate with galaxy disks or pseudobulges. *Nature*, 469:374–376.

(57) Kormendy, J. and McClure, R. D. (1993). The nucleus of M33. *AJ*, 105:1793–1812.

(58) Kormendy, J. and Richstone, D. (1995). Inward Bound—The Search For Supermassive Black Holes In Galactic Nuclei. *ARAA*, 33:581.

(59) Lauer, T. R., Faber, S. M., Ajhar, E. A., Grillmair, C. J., and Scowen, P. A. (1998). M32 +/- 1. *AJ*, 116:2263–2286.

(60) Long, R. J. and Mao, S. (2012). Made-to-measure galaxy models - II. Elliptical and lenticular galaxies. *MNRAS*, 421:2580–2592.

(61) Lucy, L. B. (1974). An iterative technique for the rectification of observed distributions. *AJ*, 79:745.

(62) Lützgendorf, N., Kissler-Patig, M., Neumayer, N., Baumgardt, H., Noyola, E., de Zeeuw, P. T., Gebhardt, K., Jalali, B., and Feldmeier, A. (2013). M - σ relation for intermediate-mass black holes in globular clusters. *A&A*, 555:A26.

(63) Lynden-Bell, D. and Rees, M. J. (1971). On quasars, dust and the galactic centre. *MNRAS*, 152:461.

(64) Lyubenova, M., van den Bosch, R. C. E., Côté, P., Kuntschner, H., van de Ven, G., Ferrarese, L., Jordán, A., Infante, L., and Peng, E. W. (2013). The complex nature of the nuclear star cluster in FCC 277. *MNRAS*, 431:3364–3372.

(65) Magorrian, J. (1999). Kinematical signatures of hidden stellar discs. *MNRAS*, 302:530–536.

(66) Magorrian, J. and Binney, J. (1994). Predicting line-of-sight velocity distributions of elliptical galaxies. *MNRAS*, 271:949.

(67) Magorrian, J., Tremaine, S., Richstone, D., Bender, R., Bower, G., Dressler, A., Faber, S. M., Gebhardt, K., Green, R., Grillmair, C., Kormendy, J., and Lauer, T. (1998). The Demography of Massive Dark Objects in Galaxy Centers. *AJ*, 115:2285–2305.

(68) Marconi, A. and Hunt, L. K. (2003). The Relation between Black Hole Mass, Bulge Mass, and Near-Infrared Luminosity. *ApJ*, 589:L21–L24.

(69) McConnachie, A. W., Irwin, M. J., Ferguson, A. M. N., Ibata, R. A., Lewis, G. F., and Tanvir, N. (2005). Distances and metallicities for 17 Local Group galaxies. *MNRAS*, 356:979–997.

(70) McLaughlin, D. E. (1995). Was the Compact Nucleus in M87 Formed by Destroyed Globular Clusters? *AJ*, 109:2034.

(71) Merritt, D., Ferrarese, L., and Joseph, C. L. (2001). No Supermassive Black Hole in M33? *Science*, 293:1116–1119.

(72) Merritt, D. and Quinlan, G. D. (1998). Dynamical Evolution of Elliptical Galaxies with Central Singularities. *ApJ*, 498:625–639.

(73) Merritt, D. and Tremblay, B. (1994). Nonparametric estimation of density profiles. *AJ*, 108:514–537.

(74) Milosavljević, M. (2004). On the Origin of Nuclear Star Clusters in Late-Type Spiral Galaxies. *ApJ*, 605:L13–L16.

(75) Morganti, L. and Gerhard, O. (2012). Regularizing made-to-measure particle models of galaxies. *MNRAS*, 422:1571–1585.

(76) Olling, R. P. (1996). NGC 4244: A Low Mass Galaxy With a Falling Rotation Curve and a Flaring Gas Layer. *AJ*, 112:457.

(77) Peterson, B. M., Bentz, M. C., Desroches, L.-B., Filippenko, A. V., Ho, L. C., Kaspi, S., Laor, A., Maoz, D., Moran, E. C., Pogge, R. W., and Quillen, A. C. (2005). Multi-wavelength Monitoring of the Dwarf Seyfert 1 Galaxy NGC 4395. I. A Reverberation-based Measurement of the Black Hole Mass. *ApJ*, 632:799–808.

(78) Rhode, K. L. and Zepf, S. E. (2001). The Globular Cluster System in the Outer Regions of NGC 4472. *AJ*, 121:210–224.

(79) Rossa, J., van der Marel, R. P., Böker, T., Gerssen, J., Ho, L. C., Rix, H.-W., Shields, J. C., and Walcher, C.-J. (2006). Hubble Space Telescope STIS Spectra of Nuclear Star Clusters in Spiral Galaxies: Dependence of Age and Mass on Hubble Type. *AJ*, 132:1074–1099.

(80) Sakamoto, K., Okumura, S. K., Ishizuki, S., and Scoville, N. Z. (1999). Bar-driven Transport of Molecular Gas to Galactic Centers and Its Consequences. *ApJ*, 525:691–701.

(81) Sandage, A. and Humphreys, R. M. (1980). On the warped optical plane of M33. *ApJ*, 236:L1–L5.

(82) Schinnerer, E., Böker, T., and Meier, D. S. (2003). Molecular Gas and the Nuclear Star Cluster in IC 342: Sufficient Inflow for Recurring Star Formation Events? *ApJ*, 591:L115–L118.

(83) Schwarzschild, M. (1979). A numerical model for a triaxial stellar system in dynamical equilibrium. *ApJ*, 232:236–247.

(84) Schwarzschild, M. (1993). Self-consistent models for galactic halos. *ApJ*, 409:563–577.

(85) Scott, N. and Graham, A. W. (2013). Updated Mass Scaling Relations for Nuclear Star Clusters and a Comparison to Supermassive Black Holes. *ApJ*, 763:76.

(86) Scowcroft, V., Bersier, D., Mould, J. R., and Wood, P. R. (2009). The effect of metallicity on Cepheid magnitudes and the distance to M33. *MNRAS*, 396:1287–1296.

(87) Sérsic, J. L. (1963). Influence of the atmospheric and instrumental dispersion on the brightness distribution in a galaxy. *Boletin de la Asociacion Argentina de Astronomia La Plata Argentina*, 6:41.

(88) Seth, A., Blum, R., Neumayer, N., Debattista, V., Cappellari, M., McDermid, R., Olsen, K., Bastian, N., Caldwell, N., Stephens, A., and Puzia, T. (2009). Surveying Nearby Nuclear Star Clusters. NOAO Proposal.

(89) Seth, A. C., Blum, R. D., Bastian, N., Caldwell, N., and Debattista, V. P. (2008). The Rotating Nuclear Star Cluster in NGC 4244. *ApJ*, 687:997–1003.

(90) Seth, A. C., Cappellari, M., Neumayer, N., Caldwell, N., Bastian, N., Olsen, K., Blum, R. D., Debattista, V. P., McDermid, R., Puzia, T., and Stephens, A. (2010). The NGC 404 Nucleus: Star Cluster and Possible Intermediate-mass Black Hole. *ApJ*, 714:713–731.

(91) Seth, A. C., Dalcanton, J. J., and de Jong, R. S. (2005). A Study of Edge-On Galaxies with the Hubble Space Telescope Advanced Camera for Surveys. I. Initial Results. *AJ*, 129:1331–1349.

(92) Seth, A. C., Dalcanton, J. J., Hodge, P. W., and Debattista, V. P. (2006). Clues to Nuclear Star Cluster Formation from Edge-on Spirals. *AJ*, 132:2539–2555.

(93) Sheth, K., Vogel, S. N., Regan, M. W., Thornley, M. D., and Teuben, P. J. (2005). Secular Evolution via Bar-driven Gas Inflow: Results from BIMA SONG. *ApJ*, 632:217–226.

(94) Shlosman, I. and Begelman, M. C. (1989). Evolution of self-gravitating accretion disks in active galactic nuclei. *ApJ*, 341:685–691.

(95) Syer, D. and Tremaine, S. (1996). Made-to-measure N-body systems. *MNRAS*, 282:223–233.

(96) Valencia-S, M., Eckart, A., Zuther, J., Fischer, S., Smajic, S., Iserlohe, C., García-Marín, M., Moser, L., Bremer, M., and Vitale, M. (2012). Discovery of an Intermediate Mass Black Hole at the center of the starburst/Seyfert composite galaxy IRAS 01072+4954. *Journal of Physics Conference Series*, 372(1):012048.

(97) van den Bosch, R. C. E., Gebhardt, K., Gültekin, K., van de Ven, G., van der Wel, A., and Walsh, J. L. (2012). An over-massive black hole in the compact lenticular galaxy NGC1277. *Nature*, 491:729–731.

(98) van den Bosch, R. C. E., van de Ven, G., Verolme, E. K., Cappellari, M., and de Zeeuw, P. T. (2008). Triaxial orbit based galaxy models with an application to the (apparent) decoupled core galaxy NGC 4365. *MNRAS*, 385:647–666.

(99) van der Kruit, P. C. and Searle, L. (1981). Surface photometry of edge-on spiral galaxies. I - A model for the three-dimensional distribution of light in galactic disks. *A&A*, 95:105–115.

(100) van der Marel, R. P., Evans, N. W., Rix, H.-W., White, S. D. M., and de Zeeuw, T. (1994). Velocity profiles of galaxies with claimed black holes. II. $f(E,L_z)$ models for M32. *MNRAS*, 271:99–117.

(101) van der Marel, R. P. and Franx, M. (1993). A new method for the identification of non-Gaussian line profiles in elliptical galaxies. *ApJ*, 407:525–539.

(102) Vasiliev, E. (2013). A new code for orbit analysis and Schwarzschild modelling of triaxial stellar systems. *MNRAS*, 434:3174–3195.

(103) Walcher, C. J., Böker, T., Charlot, S., Ho, L. C., Rix, H.-W., Rossa, J., Shields, J. C., and van der Marel, R. P. (2006). Stellar Populations in the Nuclei of Late-Type Spiral Galaxies. *ApJ*, 649:692–708.

(104) Walcher, C. J., van der Marel, R. P., McLaughlin, D., Rix, H.-W., Böker, T., Häring, N., Ho, L. C., Sarzi, M., and Shields, J. C. (2005). Masses of Star Clusters in the Nuclei of Bulgeless Spiral Galaxies. *ApJ*, 618:237–246.

(105) Wang, J., Kauffmann, G., Overzier, R., Tacconi, L. J., Kong, X., Saintonge, A., Catinella, B., Schiminovich, D., Moran, S. M., and Johnson, B. (2012). Quantifying the role of bars in the build-up of central mass concentrations in disc galaxies. *MNRAS*, 423:3486–3501.

(106) Zaritsky, D., Elston, R., and Hill, J. M. (1989). Kinematics and composition of H II regions in spiral galaxies. I - M33. *AJ*, 97:97–106.

Appendix A

Spherical Harmonics

Spherical harmonics can be considered as the angular portion of the solution to Laplace's equation in spherical coordinates. A *harmonic* is a function f that satisfies Laplace's equation

$$\bigtriangledown^2 f = 0. \tag{A.0.1}$$

The set of spherical harmonics functions is infinite and defined on a sphere, the basis functions are defined as

$$y_l^m(\theta, \phi) = \begin{cases} \sqrt{2} K_l^m \cos(m\phi) P_l^m \cos(\theta), & m \geq 0 \\ \sqrt{2} K_l^m \sin(-m\phi) P_l^{-m} \cos(\theta), & m < 0. \end{cases}$$

where the set K_l^m is the set of normalization constants

$$K_l^m = \sqrt{\frac{(2l+1)}{4\pi} \frac{(l-|m|)!}{(l+|m|)!}}. \tag{A.0.2}$$

Here l is a positive integer constant imposed by the Sturm-Liouville problem called the degree, and m is the order associated with the Legendre polynomial P_l^m which ranges from $-l, -l+1, \ldots, l-1, l$. As the spherical harmonics lie on a circle we have that $0 \leq \theta \leq \pi$ and

64

$0 \leq \phi \leq 2\pi$ and represent the angular coordinates in a general spherical coordinate system. It is important to note that

$$Y_l^{-m}(\theta,\phi) = (-1)^m Y_l^{m,*}(\theta,\phi), \tag{A.0.3}$$

where the asterisk denotes complex conjugation[7]. Spherical harmonics can be shown to be orthonormal as

$$\int_{\theta=0}^{\pi} \int_{\phi=0}^{2\pi} Y_l^m(\theta,\phi) Y_l^{m,*}(\theta,\phi) \sin(\theta) \, d\phi \, d\theta = \delta_{kl}\delta_{nm} \tag{A.0.4}$$

where δ_{ij} is the Kronecker delta.

With this set of spherical harmonics we can write any function of position $f(r)$ as

$$f(\boldsymbol{r}) = f(r,\theta,\phi) = \sum_{n=0}^{\infty} \sum_{m=-l}^{l} f_{lm}(r) Y_l^m(\theta,\phi). \tag{A.0.5}$$

where r is the radius of the function of position $f(\boldsymbol{r})$. By integrating, taking $\lim(n \to \infty)$, and using equation (A.0.3) we find

$$f_{lm}(r) = \int_{\theta=0}^{\pi} \int_{\phi=0}^{2\pi} f(r,\theta,\phi) Y_l^{m,*}(\theta,\phi) \sin(\theta) \, d\phi \, d\theta. \tag{A.0.6}$$

We can write the first few spherical harmonics as

$$l = 0, \quad Y_0^0(\theta,\phi) = \sqrt{\frac{1}{4\pi}},$$

$$l = 1 \begin{cases} Y_1^{-1}(\theta,\phi) = & \sqrt{\dfrac{3}{4\pi}} \sin(\phi)\sin(\theta), \\[2mm] Y_1^0(\theta,\phi) = & \sqrt{\dfrac{3}{4\pi}} \cos(\theta), \\[2mm] Y_1^1(\theta,\phi) = & \sqrt{\dfrac{3}{4\pi}} \cos(\phi)\sin(\theta), \end{cases}$$

$$l = 2 \begin{cases} Y_1^{-2}(\theta, \phi) = & \sqrt{\dfrac{15}{4\pi}} \sin(\phi)\cos(\phi)\sin^2(\theta), \\[2ex] Y_1^{-1}(\theta, \phi) = & \sqrt{\dfrac{15}{4\pi}} \sin(\phi)\sin(\theta)\cos(\theta), \\[2ex] Y_1^{0}(\theta, \phi) = & \sqrt{\dfrac{5}{16\pi}} (3\cos^2(\theta) - 1), \\[2ex] Y_1^{-1}(\theta, \phi) = & \sqrt{\dfrac{15}{4\pi}} \cos(\phi)\sin(\theta)\cos(\theta), \\[2ex] Y_1^{-2}(\theta, \phi) = & \sqrt{\dfrac{15}{16\pi}} (\cos^2(\phi) - \sin^2(\phi))\sin^2(\theta). \end{cases}$$